Department of Physics and Astronomy

University of Heidelberg

Master thesis

in Physics

submitted by

Daniel Winkler

born in Friedrichshafen

2020

Determination of the Krypton-Impurity Evolution in the XENON1T Detector and Optimization of Separation Columns for Krypton in Xenon Assays

This Master thesis has been carried out by Daniel Winkler

at the

Max-Planck-Institut für Kernphysik

under the supervision of

Herrn Prof. Dr. Dr. h.c. Manfred Lindner

Bestimmung der zeitlichen Entwicklung der Krypton-Verunreinigung des XENON1T Detektors und Optimierung von Trennsäulen für Krypton in Xenon Untersuchungen:

Das Ziel des XENON Experiments ist die direkte Messung von Dunkler Materie mit flüssigem Xenon als Targetmaterial. Dabei wird nach Streuereignissen sogenannter WIMPs (engl.: Weakly Interacting Massive Particles) gesucht. Da die erwartete Signalrate weniger als ein paar Ereignisse pro Jahr beträgt, ist es zwingend erforderlich, die möglichen Untergrundbeiträge zu verstehen und zu reduzieren. Zu den gravierendsten internen Untergrundbeiträgen gehört das radioaktive Kryptonisotop ^{85}Kr, das ein WIMP-Signal nachahmen kann. Allerdings kann der Kryptongehalt in Xenon durch kryogene Destillation erfolgreich reduziert werden. Die externe Überwachung des verbleibenden Kryptongehalts mit einem Edelgas-Massenspektrometer (RGMS) bildet den Rahmen dieser Arbeit. Zunächst wurde die Entwicklung der Kryptonkonzentration im XENON1T Detektor bestimmt. Eine Änderung der Signalform des RGMS erforderte ein neues Analyseverfahren, einschließlich einer stark verbesserten Fehlerbehandlung. Im Rahmen dieser Analyse wurde die niedrigste jemals in einem laufenden Detektor gemessene Krypton-in-Xenon Konzentration bestimmt. Zweitens wurden verschiedene Adsorbenzien untersucht und charakterisiert, um die Trennung von Krypton und Xenon zu optimieren, was für die vorliegende Analyse von Konzentrationen im ppq-Bereich notwendig ist. Aufgrund der gestellten Anforderungen, wie Auflösung, Peakbreite und Tailing, stellte sich die Aktivkohle "ShinCarbon" als der beste Kandidat heraus. Die ShinCarbon-Säule wird ein integraler Bestandteil eines geplanten Systems namens AUTO-RGMS sein und dabei zu einer deutlich verbesserten Trenneffizienz, einer besseren Reproduzierbarkeit und einer niedrigeren Nachweisgrenze führen.

Determination of the Krypton-Impurity Evolution in the XENON1T Detector and Optimization of Separation Columns for Krypton in Xenon Assays:

The XENON experiment aims for the direct detection of dark matter with liquid xenon as target material for so-called WIMPs (Weakly Interacting Massive Particles), which represent one of the main candidates for particle dark matter. As the expected signal rate is less than a couple of events per year, it is mandatory to understand and reduce possible background contributions. The radioactive krypton isotope ^{85}Kr is among the most serious internal background contributions, which can mimic a WIMP signal. However, krypton traces are successfully removed from liquid xenon by cryogenic distillation. The external monitoring of the remaining krypton traces using a rare gas mass spectrometer (RGMS) sets the framework of this work. First, the krypton concentration evolution of the XENON1T detector was determined. A change in the signal shape of RGMS required a new analysis procedure, including a thorough and much improved error treatment. Within this analysis, the lowest krypton in xenon concentration ever measured in a running detector is set. Second, different adsorbents were examined and characterized to optimize the separation of krypton from xenon, necessary for the present analysis of concentrations in the ppq regime. Due to the posed requirements, such as resolution, peak width, and tailing, the activated carbon ShinCarbon turned out to be the best candidate. The ShinCarbon column will be an integral part of a planned system called AUTO-RGMS and will lead to a significantly improved separation efficiency, a better reproducibility, and a lower detection limit.

Contents

1 Introduction

A wealth of observational data from gravitational effects at very different scales (cosmological and astronomical) supports the existence of a non-luminous and unknown component in our Universe. Commonly, new elementary particles are considered to be the constituents of this so-called dark matter. Such new particles arise in numerous theories beyond the standard model and could account for the observed effects. Several experiments have been conducted over the last decade, aiming to detect these massive particles. One possibility is the direct detection by measuring the scattering of a possible dark matter particle in a detector medium. This process provides information on the particle's mass and its interaction probability with ordinary matter. The XENONnT detector is operated by the XENON collaboration, using a dual-phase time projection chamber with liquid xenon as target material.
Since dark matter interactions are rare events ($<$0.01 interactions per year per kg expected) and in order to identify unambiguously interactions from dark matter particles, ultra-low background conditions are required to fulfill the goal of detecting dark matter. Hence, the suppression of interactions induced by natural radioactivity or cosmic rays is a major common challenge of all dark matter experiments. A good understanding of the sources and features of background radiation is crucial in order to be able to detect a rate excess that might be induced by a new particle. One of the most serious internal background component for detectors using liquid xenon is the radioactive krypton isotope ^{85}Kr, which is present in the liquid xenon at the trace level. It can be removed from xenon by cryogenic distillation or chromatographic separation to sub ppt level contamination. However, it is still necessary to quantify the remaining trace amounts of krypton to have precise knowledge about the detector's background conditions. To evaluate this background component, the amount of krypton in xenon has to be monitored during measurement runs. In XENONnT, this is done externally by using a rare gas mass spectrometer (RGMS), which uses cryogenic gas chromatography to pre-separate the krypton from xenon to fulfill its vacuum conditions.
After a brief introduction to dark matter and its possible detection, the XENONnT detector is presented, including its sources of backgrounds. Next, the RGMS set-up and the basics of gas chromatography are going to be explained. The main part of this thesis is divided into two parts.
In the first part, RGMS measurements of the krypton level in the XENON1T detector are analyzed. Since the current RGMS response is still not fully understood and certain features of the signal could result in significantly different outcomes, a thoroughly fit procedure was performed to achieve reasonable results with conservative errors. Last, the evolution of krypton concentration in the XENON1T detector is evaluated. In the second part, different adsorbents for the RGMS-chromatographic process are investigated. A dedicated set-up is presented to perform measurements independently of the RGMS and therefore without interrupting the system. Several adsorbents are examined and characterized to optimize the krypton-xenon separation for the RGMS.

2 Basics of Dark Matter

In this chapter, a short introduction to dark matter and its detection is given. It should be emphasized that this is not a comprehensive introduction to the field of dark matter research, it merely sets the framework of this thesis. A more sophisticated review can be found in [1] or [2–4] for a more general overview.

2.1 Indications for Dark Matter

One of the first indications for the existence of non-luminous matter was the dispersion velocities of galaxies in the Coma cluster in 1933 observed by Fritz Zwicky, who also initiated the name dark matter [5]. By using the virial theorem for a gravitational bound system, it was found that the observed high velocity dispersion of the galaxies did not match the expectation from Newtonian mechanics. Therefore it was concluded that the visible mass was not enough to account for the observed velocities and to hold the cluster together gravitationally.
This was further confirmed by the measurement of rotation curves of various spiral galaxies by Rubin et. al. [6]. The investigated angular velocity for various distances from the galactic center showed significant deviations from the expected $r^{-1/2}$ dependence of the rotational velocities with larger distance to the galactic center. Instead, the velocities stay constant for regions far outside of the galaxy. This behavior can be explained when an extended uniform halo of dark matter around the galaxy is assumed. Dark refers here to the absence of any electromagnetic interaction, including the emission of photons.
Another observational evidence is gravitational lensing [7]. In analogy to optical lenses, light is deflected when passing through a large gravitational potential, resulting in e.g. deformations or multiple images. By measuring the deflection of the light, the total mass of the object causing the distortion can be reconstructed, proving that luminous matter alone does not account for the enclosed mass potential [8]. This method is also used to study the collision of two galaxy clusters, e.g. the Bullet Cluster [9]. Using weak gravitational lensing, it was observed that the reconstructed gravitational centers of dark matter are clearly displaced from the center of luminous matter. The displacement of the gravitational centers is explained by collisions of baryonic matter and a very small or non-existent self-interaction of dark matter [10].
So far only indications for dark matter on astronomical scales were presented. The most compelling evidence for the existence of dark matter comes from cosmological arguments. The discovery of the Cosmic Microwave Background (CMB) and its imprinted temperature fluctuations [11] is the foundation for the cosmological Standard Model [12]. This model is able to describe the anisotropies of the CMB temperature with very high accuracy. Since these anisotropies are, amongst others, dependent on the composition of the universe (baryonic matter, non-baryonic matter, dark energy), the most recent measurement [13] requires that a large fraction of the matter content of the universe is made up by dark matter. In particular $\sim 26.5\%$ dark

matter and $\sim$ 4.8% ordinary baryonic matter (matter described within the Standard Model of particle physics), while the rest consists of dark energy. This result is remarkably consistent with the value of the baryonic mass density obtained from the Big Bang Nucleosynthesis (BBN) [14].
Directly linked to the structure of the CMB is the influence of dark matter on large structure formation in the universe. Simulations on the large scale structure of the universe use these density fluctuations as seeds for structure formation. They show that our observations of large scale structures can be produced by non-relativistic (cold) dark matter [15, 16].

2.2 Properties and Candidates

To explain these observations, new theories, such as the modification of gravitational laws (e.g. STVG [17], TeVeS [18]), or objects that produce very little to no light, e.g. primordial black-holes [19] or massive astrophysical compact halo objects [20], arose. These theories either lack to explain all of the observed phenomena or are ruled out by observations to make up for the entire dark matter content [20]. Therefore, dark matter as a particle is a favorable candidate, since additionally, various observations indicate that the standard model needs to be extended.
The hypothetical particle has to fulfill certain constraints to be compatible with the mentioned observations [21]:

- massive $\rightarrow$ interact gravitationally
- electrically neutral
- weakly or sub-weakly interacting
- stable or long-lived
- cold or warm $\rightarrow$ non-relativistic velocity
- majority non-baryonic

Its baryonic nature can be ruled out by the CMB and BBN models. The electromagnetic interaction is excluded by the absence of light absorption or electromagnetic interactions with the interstellar medium. Since the gravitational effects of dark matter affect the Universe from its early stage on until today, a dark matter candidate needs to be stable, or, if unstable, its lifetime must be long with respect to the age of the Universe. Dark matter particles must be non-relativistic, i.e. cold, for them to be able to take part in the structure formation in the Universe. Finally, the self-interaction of a dark matter candidate needs to be, if at all, very weak (see remarks on "Bullet Cluster" in the previous section).
A promising candidate in the Standard Model would have been the neutrino. Cosmological simulations have shown, however, that a Universe dominated by neutrinos (highly relativistic, hot) would not be in agreement with the observed clustering

scale of galaxies. Also, their total number is too low to constitute the mass needed for them to be viable dark matter candidates. Thus, they cannot account for the observed dark matter density.
In various extension of the standard model, also addressed to different physical problems, (e.g. super-symmetry), several hypothetical elementary particles are predicted that could fall into this class of a dark matter candidate [22]. Examples are axions and axion-like-particles [23], or sterile neutrinos [24].
Among the most promising dark matter particle candidates are the so-called weakly interacting massive particles (WIMPs), which are predicted by several super-symmetric extensions to the standard model. A WIMP is a new elementary particle, which interacts via gravity and potentially the weak nuclear force. Moreover, it could interact with any other force not part of the Standard Model itself, which is as weak as or weaker than the weak nuclear force. Possible WIMP candidates are the lightest particle in the Kaluza-Klein theory [25] or the lightest neutralino in SUSY models [22]. Furthermore, the predicted self-annihilation WIMP cross-section at the scale of the electroweak interaction and the assumption of thermal production results in the correct abundance of dark matter observed today as thermal WIMP relics of the big bang [26]. The WIMP is, therefore, a theoretically well-motivated dark matter candidate. More details on dark matter candidates are summarized in [1, 3, 27, 28]. In the following, dark matter is considered to be described as a WIMP.

2.3 Detection Principles

If indeed, particles are the answer to the dark matter puzzle, there are three main possibilities for a discovery as illustrated in Fig. 1.

1. Production at particle colliders e.g. $pp \rightarrow \chi\chi$.

2. Looking for products of their self-annihilation at locations with a high dark matter density (indirect detection) e.g. $\chi\chi \rightarrow e^+e^-$.

3. Measurement of the scattering of a dark matter particle off a target material (direct detection). In the case of the WIMP, this is the scattering off atomic nuclei.

In a collider, it is attempted to produce dark matter particles by the collision of Standard Model particles. Most candidates, e.g. WIMPs, are considered to be stable and having a very small cross-section. After their creation, dark matter particles will leave the detector undetected, similar to neutrinos, leading to a missing transverse momentum in the signal [29].
Indirect detection searches look for the annihilation of dark matter particles into Standard Model particles. Experiments following this detection strategy are typically looking for gamma-rays, neutrinos or anti-particles (e.g. positrons) produced in the annihilation process. The highest annihilation rate is expected from regions with a high dark matter density, for example, the center of galaxies or the Sun [30].

In a direct detection experiment, the goal is the direct proof of the scattering process of a WIMP particle off ordinary matter, e.g. an atomic nucleus. The principles of direct detection and expected recoil rates are summarized below.

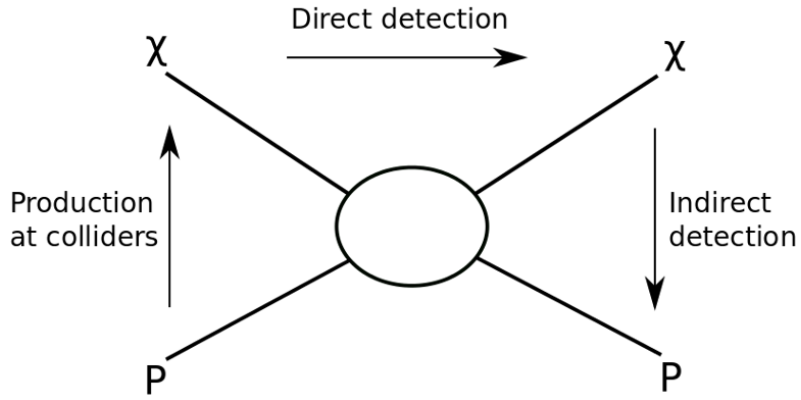

Figure 1: Schematic representation of dark matter coupling to standard model particles. In the upwards direction, dark matter particles are created from the annihilation of standard model particles, and can thus be produced in the collisions of e.g. protons. The downwards direction represents the opposite process, where dark matter particles can be detected indirectly by their annihilation into standard model particles. The direct detection channel is given by the horizontal direction; here dark matter particles can be detected directly by their interactions when scattering off standard model particles [1].

2.4 Direct Detection

2.4.1 Experimental Signature

By conducting a direct detection experiment such as XENONnT, one is interested in the event rate of the process under investigation [1, 31, 32]. The following equation shows the differential rate of the recoil energy dR/dE_R, where ρ_0 is the dark matter density, M the total target mass, m_N the target nuclei mass and σ the interaction cross-section.

$$\frac{dR}{dE_R} = \frac{\rho_0 M}{m_\chi m_N} \int_{v_{min}}^{v_{esc}} v f(v) \frac{d\sigma}{dE_R} dv$$

There are three contributing parts to the equation. The detector parameters, the astrophysical input, and the particle physics part:

1. The detector parameters (M, m_N, v_{min}) mainly come from the target material and its amount. Furthermore, the energy of the recoil depends predominantly on the velocity of the incoming WIMP. Since a detector has an energy threshold, which is the lowest value it can measure, there has to be a minimal velocity v_{min} of the WIMP for the recoil to be measured.

2. The scattering in direct detection experiments is induced by particles from our galaxy's dark matter halo. The distribution and kinematics of the dark matter particles, therefore, govern the expected signal and are thus essential for the interpretation of the expected rate. The exact distribution could not yet be measured; however, it can be modeled using the knowledge derived from gravity-based observations. The model which is commonly used (Standard Halo Model [33]) assumes that the dark matter particles have a Maxwellian velocity distribution $f(v)$, which is truncated at the escape velocity v_{esc} of the galaxy.
   Other effects that have to be considered for the velocity are the rotation of the Earth around the Sun and the inclination angle between the Earth's orbit and the galactic plane. These details lead to two observational consequences:
   - annual modulation: The velocity of the dark matter relative to the Earth is largest around June and smallest in December. Consequently, the amount of particles able to produce nuclear recoils above the detector's energy threshold varies over the year. This effect is of the order of 3%.
   - directionality: The differential rate depends on the angle between the direction of the recoil relative to the direction of the solar motion. The rate of events is, therefore, directional dependent and the Earth's daily rotation thus constantly changes the signal direction observed in a detector.

3. The total cross-section for the scattering of WIMPs off target nuclei can be separated into a spin-independent (SI) and spin-dependent (SD) part. Both are possible since we do not know how the WIMP interacts with ordinary matter. It is therefore important to perform independent studies with different target nuclei to probe both quantities. The SI cross-section is proportional to the mass number and the SD one to the total angular momentum of the nuclei as well as the expectation value of the spin of the proton or neutron.

Taking all this into consideration, typical event rates below one event per kilogram per year are expected. This is further complicated by the fact that the measured recoil energy is very low. For a WIMP mass of about 10 GeV to 1000 GeV nuclear recoils in the range of 1 keV to 100 keV result. Keeping this in mind, the optimal WIMP detector consists of:

- a large total mass
- a target nuclei with high mass number
- a low energy threshold
- an ultra-low background
- the ability to distinguish signal from background events

2.4.2 Detector Signal

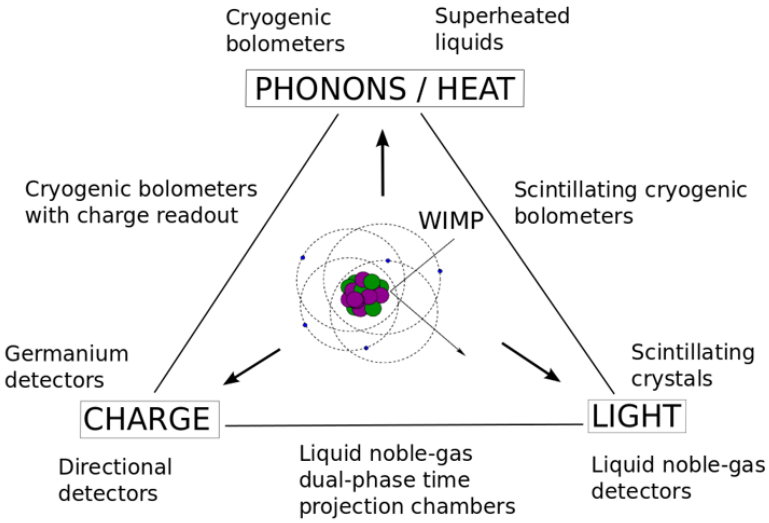

Figure 2: Illustration of different detection signals and the detector techniques to use a combination of two [1].

The nuclear recoil can be detected by the effect of a nucleus moving through a medium, which can create ionization, excitation, and heat [1]. In most dark matter experiments, a combination of two detection channels is used. The response of some media to an interaction is not only proportional to the deposited energy but depends on the type of particle that deposits the energy. Therefore, recoils from different particles can be separated (discrimination). In Fig. 2 the three detection signals and the respective technology for their measurement are shown. For a detailed review of different detector technologies see [1, 34]. The XENONnT detector which is presented in the next section belongs to the liquid noble gas detectors combining charge and light signals.

2.4.3 Dark Matter Search Results

Results are displayed in the dark matter-nucleon cross-section versus the dark matter mass parameter space (Fig. 3). In the derivation of these properties from the measured rate, the astrophysical values for the dark matter density and its velocity distribution as well as an interaction model have to be assumed. A possible detection would be displayed as a contour region representing a certain confidence level. If there is no indication an exclusion plot is drawn, which show the upper limit of the cross-section versus the mass:

- The low-energy threshold of the detector is mainly responsible for the reduced sensitivity at low WIMP masses.

- The minimum of the exclusion curve is given by the kinematics of the scattering process which depends on the target nucleus mass.
- At larger WIMP masses, the event rate is overall suppressed by $1/m_\chi$which is explained by the fact that the local dark matter density is constant. Consequently, the heavier the individual particle, the fewer particles are available for scattering. In addition, the form factor, which accounts for the extension of the nucleus, reduces the rate for interactions with large momentum transfer.

2.4.4 Research Status

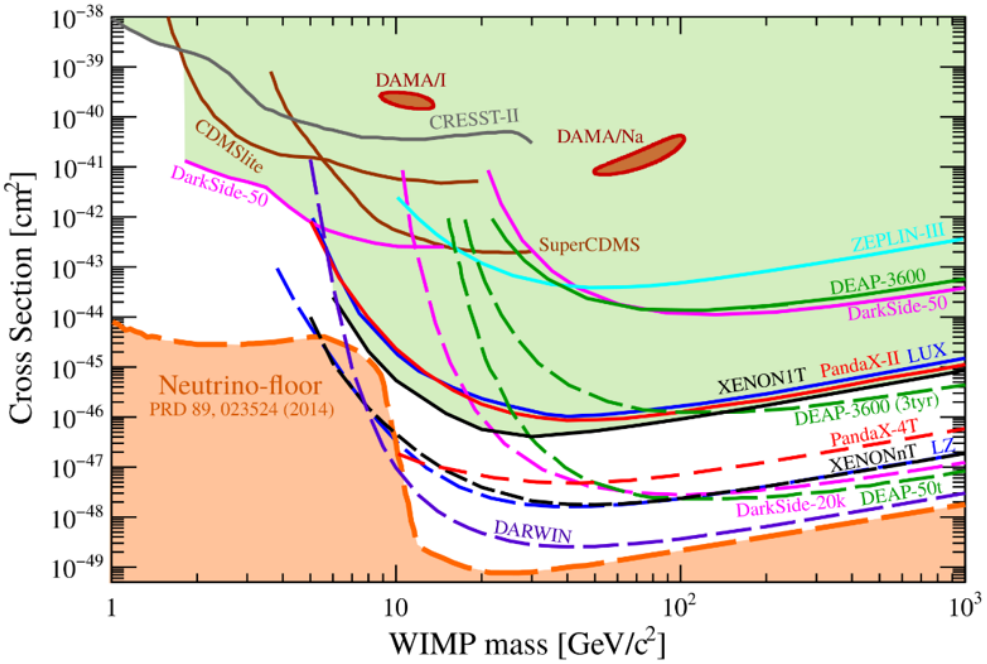

Figure 3: Current results of various direct detection experiments searching for WIMPs. Their exclusion limits are shown as solid lines. The dashed lines indicate the estimated exclusion plots of planned experiments [35].

The current status of the search for spin-independent WIMP-nucleon scattering is shown for various experiments in Fig. 3 (solid lines). Above WIMP masses of $5\,\mathrm{GeV/c^2}$, the strongest limits are placed by XENON1T. It excluded spin-independent WIMP-nucleon interactions with cross sections above $4.1 \cdot 10^{-47}\mathrm{cm}^2$ at $30\,\mathrm{GeV/c^2}$ [36].
Cryogenic experiments using germanium- or scintillating-crystals using ionization and phonons or light and phonons, respectively, cannot compete in the search for this WIMP mass range, which is due to their much smaller target mass and higher backgrounds. Yet, they are very sensitive to low mass WIMPs due to their extremely low thresholds.

Furthermore, there is some inconsistent data from the DAMA experiment, showing a signal contour, indicating a discovery of a dark matter particle. This measurement is not confirmed by any other experiment and even excluded by various experiments by orders of magnitude of cross-section.
For a more profound review of the status of the dark matter search, one is referenced to the current literature.

3 The XENON Dark Matter Experiment

Among the various direct dark matter detection techniques, liquid noble gas time projection chambers (TPCs) have been proven to be the most successful. The XENON collaboration is operating this kind of detectors since the early 2000s aiming to solve the dark matter mystery with main focus on the WIMP search [37–39]. The latest results are from the XENON1T detector, which is, similar as its precursors, located in the underground facilities of the INFN Laboratori Nazionali del Gran Sasso (LNGS) in Italy, shielded from cosmic muons by $\sim 1.4\,\mathrm{km}$ of rock ($\sim 3.6\,\mathrm{km}$ water equivalent) [40]. The XENON1T detector is one of the most sensitive devices, setting the lowest upper limits on the spin-independent WIMP-nucleon cross-section for WIMP masses above $\sim 5\,\mathrm{GeV/c}$ [36]. Its successor XENONnT, which is currently in commissioning, is aiming to exclude cross-sections down to $\sim 2 \times 10^{-48}\,\mathrm{cm}^2$ [41], enabling it to probe the WIMP dark matter parameter space with unprecedented sensitivity.
In the subsequent section, the working principle of a dual-phase TPC will be described followed by an overview of the XENONnT detector set-up. Then the dominating background sources for dark matter searches with XENON are explained.

3.1 The Dual-Phase LXe TPC, Detection Principle

As the name already implies, the detection medium is xenon which offers several advantages. The ionization and scintillation properties of xenon should enable the detection of WIMPs and their discrimination from background. The high atomic number enhances the cross-section for spin-independent interactions. Moreover, xenon has a high stopping power which provides a good self-shielding capacity for background reduction.
The detection principle is the so-called dual-phase (liquid and gaseous xenon) **T**ime **P**rojection **C**hamber (TPC), which allows for the observation of both the light and charge signals induced by particle interactions. The detection principle of XENON is illustrated in Fig. 4.
The detector consists of a large cylindrical liquid xenon phase corresponding to the actual target and a smaller gaseous phase at the top. On top and bottom of the detector, arrays of photomultiplier tubes (PMTs), immersed into the liquid and gas phase, are employed. A particle interaction (e.g. scattering of a WIMP off a xenon nucleus) in the liquid xenon target produces excited and ionized atoms [38]. The excited xenon combines with neutral atoms forming excimer states [42], which subsequently decay under the emission of ultraviolet light. This prompt scintillation light is measured by the arrays of PMTs and is called S1. A high fraction of the S1 signal is detected by the bottom array due to the high internal reflection of the scintillation light at the liquid-gas interface. The ions form singly ionized molecules with neutral atoms. These would also recombine in several steps to form excited xenon atoms if the ionization electrons are not removed. Instead, a fraction of the charge is separated from the interaction site with an electric field applied between

the cathode and a grounded gate electrode, which are located above the bottom array and at the liquid-gas interface. Thus the electrons drift upwards to the xenon gas phase above the liquid. Using a second, stronger electric field, applied between the gate electrode and the anode in the gas phase, these electrons are then extracted into the gaseous xenon. The second electric field provides the electrons with enough energy to excite the xenon atoms and generate a secondary scintillation light signal by colliding with the gas atoms (electroluminescence) [43]. This signal is called S2 and is proportional to the amount of charge liberated by the interaction. The S2 signal is as well observed by the arrays of photomultiplier tubes.

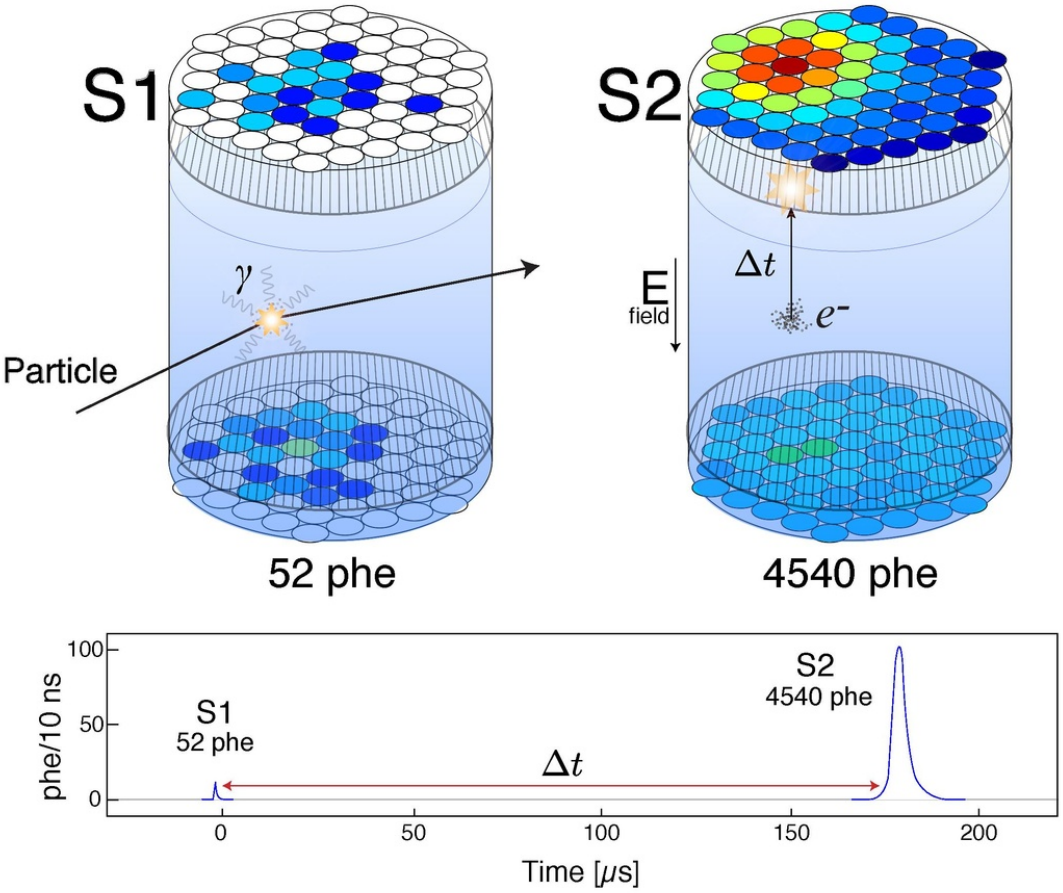

Figure 4: Illustration of the detection principle: The scintillation light emitted by the excited atoms is measured by the PMTs (left). The electrons from ionized atoms are extracted by drifting them upwards in the gas phase, where they produce a second scintillation light (right). At the bottom, the size of the two signals as well as there time separation is shown, which are used to reject background [44].

By the simultaneous detection of the two signals, a 3-dimensional reconstruction of the event vertex in the TPC is possible. The z-coordinate is obtained from the time difference between the S1 and S2 signal [45] as illustrated at the bottom of

Fig. 4. The x,y-coordinates can be accessed by the hit pattern in the PMTs. The S2 signal is located very close to the origin of the secondary scintillation light and shows thus distinct patterns for different event locations. Resolution in the mm regime is achieved for all three spatial coordinates. This is crucial for defining a fiducial volume in the detector in order to reduce the number of events induced by radioactive radiation from surrounding materials. Moreover, the partition into excitation and ionization depends on the particle type and therefore provides several means to reject radioactive backgrounds, which are further explained in Sec. 3.3. Due to this ability, the XENON detectors achieve very low background conditions.

3.2 The XENON Detector Set-up

3.2.1 The XENON1T Detector

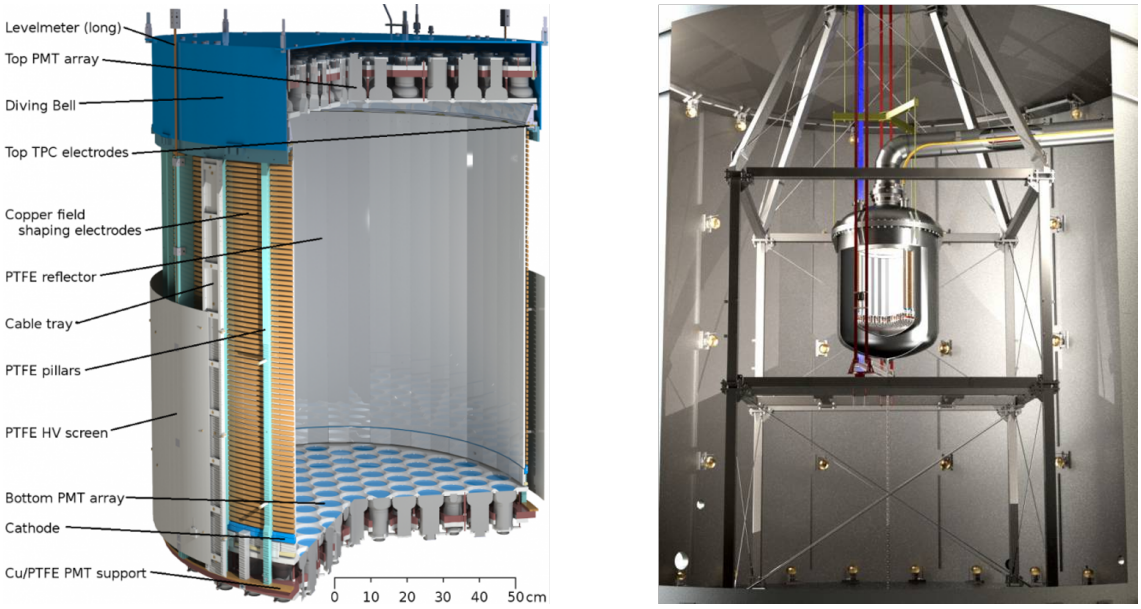

Figure 5: The XENON1T experiment. (Left) CAD drawing of the XENON1T TPC. (Right) CAD drawing of the TPC housed inside the cryostat, situated in the water tank acting as an active muon veto [39].

As mentioned before, the XENON1T detector is located at the Gran Sasso Underground laboratory. The detector uses in total 3.2 t of ultra-pure liquid xenon, where 2 t are used as target volume. The cylindrical TPC, shown in Fig. 5 left, shows a height of $\sim$ 1 m and a radius of $\sim$ 1 m. The top and bottom PMT arrays are equipped with 127 and 121 PMTs. The PMTs of the bottom array are arranged hexagonally to maximize the light collection efficiency, the top PMT array is optimized for a good radial resolution of the xy-position reconstruction. The walls of the TPC are covered by Teflon panels to increase the light yield. The panels are surrounded by field-shaping electrodes made from low-radioactivity copper in a ring

structure, designed to keep the drift field as uniform as possible over the whole drift length. The drift and extraction fields are generated by a cathode, a gate grid and an anode. The gas phase on the top of the TPC is created by a constant stream of gaseous xenon into a diving bell structure, thus pressurizing it. A vertically movable gas exhaust tube allows to release pressure into the liquid from outside of the TPC and thus adjust the liquid level inside the bell.
The entire TPC structure is housed inside a double-walled cryostat, with the inner and outer walls vacuum isolated. It should thermally decouple the inner vessel from ambient temperature to keep the liquid xenon at a temperature of 180 K.
As shown in Fig. 5 the cryostat is placed in the center of a 9.6 m diameter water tank used both as a shield and as an active Cherenkov muon veto with 4π coverage [46]. The inner walls of the water tank are covered with a foil that is highly reflective in a large range of photon wavelengths so that they can be detected by the PMTs installed inside the water tank. The PMTs inside the water tank will detect Cherenkov light and generate a logical veto to discriminate against high energetic muons and is thus able to detect more than 99.5% of the residual cosmic muon flux at the LNGS underground laboratory [46]. Hence, muons and muon-induced background can be tagged and their contribution to the background is negligible [47]. More information on the background and its reduction strategies in the XENON experiment is given in Sec. 3.3.
The XENON1T gas system contains several subsystems necessary for regular operation. The auxiliary systems are located on three floors of a support infrastructure building next to the water tank. They comprise:

- the cryogenic system providing the cooling power by utilizing pulse tube refrigerators, keeping the xenon in the TPC liquid
- the gaseous xenon purification system for the removal of water and electronegative impurities, e.g. oxygen, via two hot getters
- the cryogenic distillation column of $\sim$5 m height for krypton removal
- a spherical xenon storage and recovery vessel (ReStoX) of 1 m diameter, able to store up to $\sim$7.6 t of liquid or gaseous xenon
- a bottle rack connected to a gas analytics system, providing the interface to the other detector subsystems during the injection of new xenon from gas bottles
- the data acquisition system (DAQ) and a control room from which the detector can be operated.

The water tank and the building containing the auxiliary systems are shown in Fig. 6. For more detailed descriptions and supplementary information on the sub-systems, one is referred to [39].

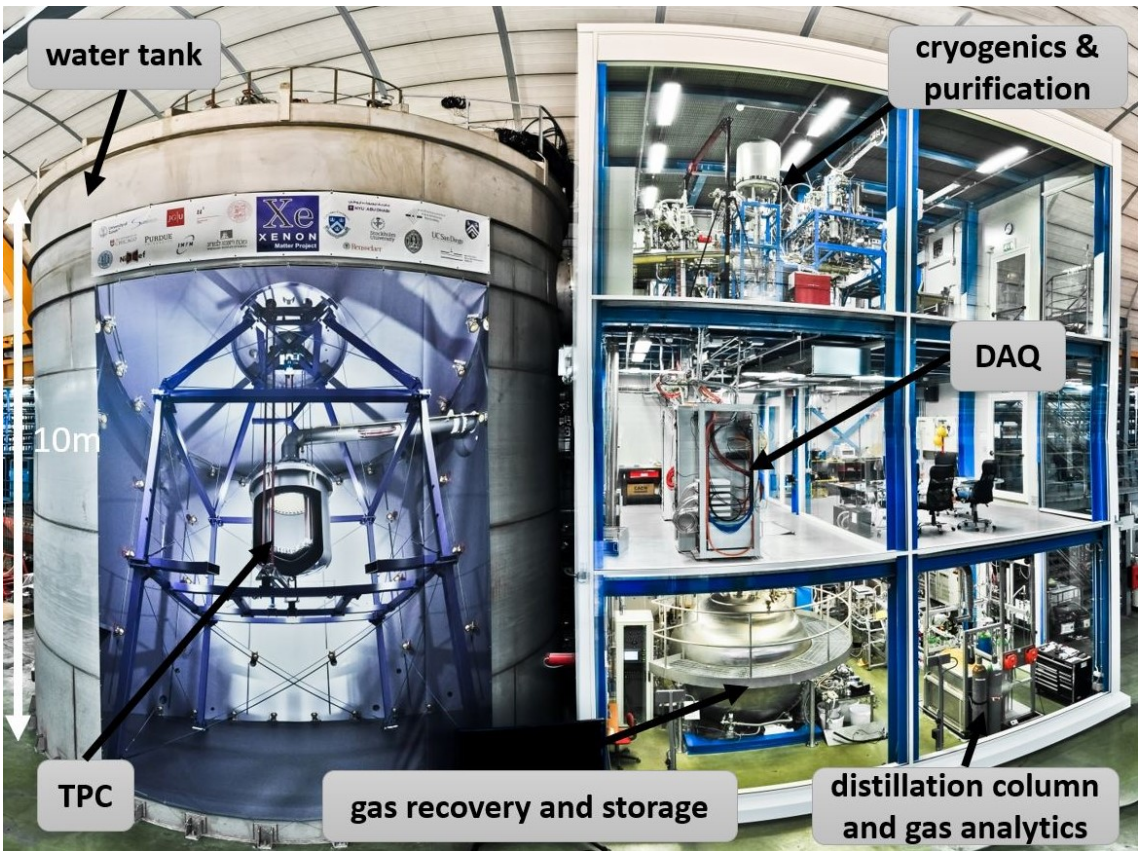

Figure 6: Water tank containing the cryostat next to a three storage building, housing the auxiliary systems [48].

3.2.2 The XENONnT Detector

The next phase of the XENON experiment will be the XENONnT detector [41], which is currently in commissioning. It is also located at the INFN Laboratori Nazionali del Gran Sasso and reuses the main infrastructure, the support systems as well as the water tank and outer cryostat of XENON1T. To further reduce background sources (Sec. 3.3), in order to achieve higher sensitivity levels, some upgrades and new developments are implemented in addition to a larger TPC.
The XENONnT detector will feature an active target mass of 5.9 t of LXe in a TPC of ∼1.5 m height. The PMT arrays will be equipped with 253 top and 241 bottom PMTs of the same type as used in XENON1T. Similar as in XENON1T they are arranged in a compact hexagonal structure to maximize light collection efficiency.
The upgrades include an improved GXe purification system. In addition to the krypton distillation column, which is reused from XENON1T [49], a second newly developed radon column is added [50]. To be able to store and recover the entire amount of about 8 t of xenon in the system, a second and larger xenon storage vessel (ReStoX2) is constructed. Finally, the innermost part of the water tank around the cryostat housing will be optically separated from the rest of the water tank and

transformed into an active neutron veto. The XENONnT neutron veto will reduce the radiogenic neutron background by tagging events where the interaction in the TPC is coincident with a detected neutron. In order to enhance the neutron detection probability via neutron capture, the water within the muon veto tank is loaded with gadolinium sulphate octahydrate. The muon veto system, containing $\sim 700\,\mathrm{t}$ of Gd-loaded water, is inherited from XENON1T.
In total XENONnT consists of three nested detectors: the central LXe TPC, surrounded by the Gd-loaded water neutron veto and the outer optically separated muon veto in the water tank. A schematic picture of the nested detector set-up is shown in Fig. 7.

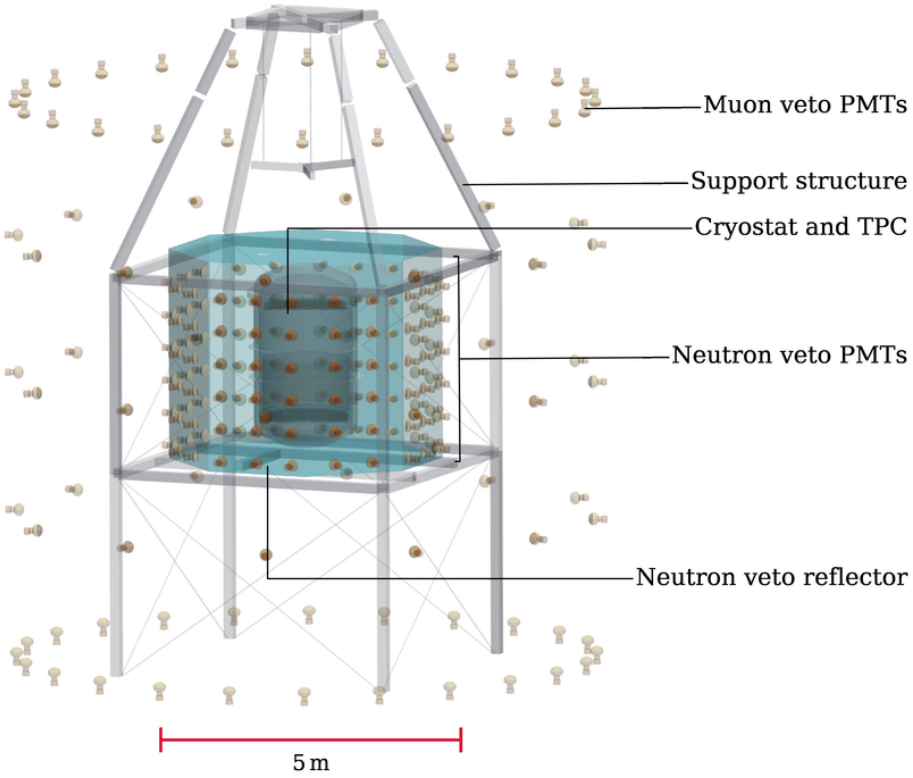

Figure 7: Rendering of the three nested detectors, including muon and neutron veto. The optical separation is shown as a transparent turquoise surface [41].

The ultra-low XENON1T background level will be further reduced in XENONnT by the improved purity of the xenon inventory and the aforementioned upgrades and additions.
With the exposure goal of 29 ty, the expected sensitivity to spin-independent WIMP-nucleon interactions reaches a cross-section of $1.4 \times 10^{-48}\,\mathrm{cm}^2$ for a $50\,\mathrm{GeV/c}^2$ mass WIMP at 90% confidence level [41], which is more than one order of magnitude beyond the current best limit, set by XENON1T.

3.3 Background Sources and Reduction Strategies

In order to identify unambiguously interactions from dark matter particles, one of the most important tasks in dark matter direct detection is the reduction and discrimination of background. WIMP-nucleus scattering is a rare event, thus it is necessary to obtain ultra-low background conditions and to model and quantify all possible sources of background. The background sources of detectors using liquid xenon as detection medium like the XENON experiments can be categorized by the signature they leave in the detector, i.e. electronic or nuclear recoils. Furthermore, they can be divided into internal or external backgrounds, depending on whether the source is inside or outside of the detection medium.

3.3.1 Internal Background

The internal background includes sources that are within the xenon itself. Xenon contains trace amounts of krypton, especially the radioactive isotope ^{85}Kr, as well as radon, emanated from surrounding materials [47]. Since these impurities distribute homogeneously within the liquid xenon, this background can not be reduced by fiducialization (see Sec. 3.3.3).
Radon (^{222}Rn) is the only gaseous isotope in the decay chain of ^{238}U, which is naturally present in most detector materials. As a noble gas, radon constantly emanates and dissolves into the liquid xenon volume and contributes to the background by the β-decays of its daughters, mainly ^{214}Pb. This background can be reduced by a careful selection for low-radioactivity materials with a low radon emanation to be used in the detector construction. Furthermore, a radon distillation column in the purification system is utilized to further suppress radon backgrounds [41].
Xenon is commercially produced by extraction from air. The natural abundance of xenon in air is 0.09 part per million by volume (ppm), while krypton has a volume concentration of 1.14 ppm. Xenon and krypton are separated by fractional distillation, but the limited efficiency due to the inert properties of these two noble gases causes traces of krypton in commercially available xenon of part per million (ppm) to part per billion (ppb). The two main krypton isotopes are ^{84}Kr and ^{86}Kr with the relative abundances of 57% and 17.5%, respectively. Although natural krypton has no radioactive isotope which could be dangerous in terms of background, it contains the isotope ^{85}Kr at a level of $\sim 10^{-11}$ [51]. The radioactive krypton isotope ^{85}Kr is produced by man-made nuclear fission and released during nuclear weapon tests and in nuclear fuel reprocessing plants. It is an almost pure β-emitter with an endpoint energy of 687 keV and a half-life of 10.76 years. With these properties it is a source of a permanent, uniformly distributed background causing electronic recoils.
The average atmospheric concentration of ^{85}Kr is approximately constant since 2005 with a value of 1.5 Bq/m^3 [52]; concentrations are higher locally around nuclear reprocessing facilities. Unfortunately, there are no detailed measurements of the ^{85}Kr activity in Italy available. The average value of 1.5 Bq/m^3 activity at LNGS is assumed, which is supported by a measurement of (1.3 ± 0.2) Bq/m^3 taken from [51].

This results in a ratio of ^{85}Kr in natural krypton of $^{85}\mathrm{Kr}/^{nat}\mathrm{Kr} \sim 2.0 \times 10^{-11}$ [53]. The anthropogenic ^{85}Kr can be successfully removed from xenon with cryogenic distillation by a dedicated krypton distillation column (see Sec. 4.1 for more details) [49]. This is done before filling the xenon into the detector as well as a continuous online distillation. For the prediction of the krypton induced internal background, its concentration is determined by *Rare Gas Mass Spectrometer (RGMS)* measurements, which is presented in the next chapter. For the case of the XENON1T detector, the lowest achieved krypton level was $^{nat}\mathrm{Kr/Xe} = (0.36 \pm 0.06)$ ppt [39].

3.3.2 External Background

The external background includes natural radioactivity (e.g. γ- and β-radiation) from the environment and from the materials used to build the detector as well as cosmic radiation (e.g. neutrons and muons).
The most important background source for WIMP detection are nuclear recoils induced by neutrons, as they are fundamentally indistinguishable from WIMP interactions. Cosmogenic neutrons are produced due to spallation reactions of muons on nuclei in the experimental setup or in the surrounding rock. Losing energy while penetrating into the detector, they can induce low-energy nuclear recoils in the WIMP search region. In addition, neutrons are produced in spontaneous fission reactions caused by natural radioactivity.
To shield the experiment from cosmic radiation, the XENON experiment is placed in the LNGS underground laboratory, where the atmospheric muon flux is reduced by about 6 orders of magnitude [1]. As mentioned before, the water tank of the XENONnT detector acts as a muon veto. Additionally, the water tank provides shielding from natural radioactivity outside the experimental setup. To reduce the background from natural radioactivity within the setup, detector components close to the sensitive volume are screened beforehand to select radio-pure materials [1].
To even further reduce the neutron background the upgrade from XENON1T to XENONnT includes a neutron veto. Neutrons that scatter in the TPC volume can easily pass through the cryostat and escape further detection in LXe. Neutrons that leave the TPC volume will be moderated by the water around the cryostat. After being thermalized and captured by gadolinium, a gamma-ray cascade is generated. The deposited energy by the gammas is ultimately transformed into Cherenkov photons, which are detected by PMTs and a logical veto signal is produced. The neutron veto will enable the identification of otherwise irreducible neutron backgrounds in the target volume [41].
The only background source that can not be avoided or shielded are neutrinos, mainly originating from the sun. They can produce an electronic recoil by elastically scatter off electrons as well as a nuclear recoil by coherent neutrino-nucleus elastic scattering. This so-called neutrino-floor will be the ultimate limit for WIMP detection with the LXe TPC principle as shown in Fig. 3.

3.3.3 Background Discrimination

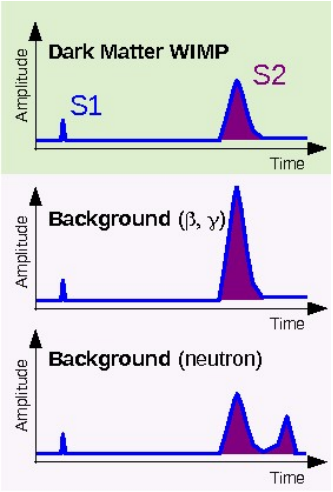

Figure 8: Signature of a possible WIMP (top), a background event from β- or γ-radiation (center) and neutron with multiple scattering (bottom). The ratio S2/S1 can be used to distinguish signal from background events [39].

Even with such a low background level as XENONnT, background discrimination is necessary to further distinguish signal from background events. First of all, the probability of dark matter particles to interact is so low, events with multiple simultaneous hits in the target volume, as for example possible for neutrons producing two S2 signals (Fig. 8 bottom), can be excluded.
Additionally, since the detector is sensitive to the position of the interaction, an innermost volume can be selected for the analysis, called fiducial volume. This has the effect that the background is effectively suppressed because the penetration range of radiation has an exponential dependence on the distance (self-shielding of xenon). Therefore, most background interactions take place close to the surface. However, this has a smaller effect in neutron background reduction due to their larger mean free path compared to gamma-rays.
Finally, the detector is able to distinguish electronic recoils from nuclear recoils. The energy loss in liquid xenon is different for electronic recoil events from γ- or β-background interaction and for nuclear recoil events from a potential WIMP signal or a neutron [54]. The energy partition into excitation and ionization varies for the two types of recoil. Consequently, the ratio of the charge to the light signal (S2/S1) is different for both types. In other words, the ratio of the two signals depends on the particle type and allows to separate signal events from background events as indicated in Fig. 8 (top and center). Due to the high rejection this usually renders the electronic recoil background subdominant, even though it is usually dominating the overall background budget. Electronic recoils can still be misidentified as WIMP interactions, since the energy partition of electronic and nuclear recoil overlap (discrimination power $\sim 99.5\%$ [55]).

4 Krypton in Xenon Quantification

4.1 Motivation

Krypton in form of ^{85}Kr is one of the main internal background sources for xenon detectors as described in Sec. 3.3.1. The electrons emitted from decaying ^{85}Kr atoms inside the liquid xenon target cause electronic recoils. As mentioned in Sec. 3.3.3, most of these background events can be excluded from the data with a discrimination power of ∼99.5%. However, the remaining ∼0.5% of ^{85}Kr decays are indistinguishable from possible WIMP interactions. Permitting ∼13 events per tonne per year (assuming 4 t fiducial volume of XENONnT and a region of interest of (1,13)keV [41]) arising from this background source, simulations show that the krypton concentration inside the liquid xenon target has to be below 0.1 ppt. This low concentration is achieved with a dedicated cryogenic distillation column:
The separation is achieved by exploiting the difference in vapor pressure. Since at the same conditions the vapor pressure of krypton is higher than that of xenon, a higher concentration of krypton will be in the gaseous phase than in the liquid phase, after equilibrium is reached. Simplified, a distillation column is a series of such separation stages. Thus, the krypton concentration in the liquid phase decreases successively with each stage. The krypton enriched off-gas is collected at the top of the column, while the purified liquid xenon is collected at the bottom. For the technical specifications of the distillation column and the detailed description of the working principle see [56, 57]. The column developed for XENON1T using this method reduced the ^{nat}Kr concentration by 5 orders of magnitude [57].
The purification of xenon to such low impurity concentrations has to be confirmed and evaluated by dedicated analytic methods of krypton in xenon concentrations down to the ppq level. This is performed offline, i.e. xenon samples are drawn from the detector and analyzed by a dedicated set-up. The Xenon Collaboration uses a gas-chromatographic rare gas mass spectrometer (RGMS), which is located at the Max-Planck-Institut für Kernphysik in Heidelberg. This device sets the framework of this thesis and is described in this chapter.

4.2 The RGMS Set-Up

4.2.1 Detection of ^{85}Kr

A direct measurement of ^{85}Kr in a sample with a krypton concentration in the sub-ppb regime is not feasible, since this would require either a huge xenon sample or a technique to detect single ^{85}Kr atoms. However, the ratio of ^{85}Kr/^{nat}Kr is relatively known (Sec. 3.3.1). This makes it possible to transfer the determination of the ^{85}Kr amount to the measurement of the abundances of stable krypton isotopes like ^{84}Kr and ^{86}Kr. Therefore, the measurement does not rely on the detection of radioactive decays.

4.2.2 Experimental Set-Up

The RGMS, as a set-up to measure krypton in xenon traces, was designed, constructed and thoroughly characterized during the work of [58]. It consists of two main parts, a mass spectrometer for detection and a cryogenic gas-chromatography system for sample preparation. Additionally, the setup features various sub-systems such as ports for calibration purposes, getter modules and pumping sections. A simplified sketch of the set-up is shown in Fig. 9. The individual parts are explained below and follow closely the descriptions in previous works [58–61].

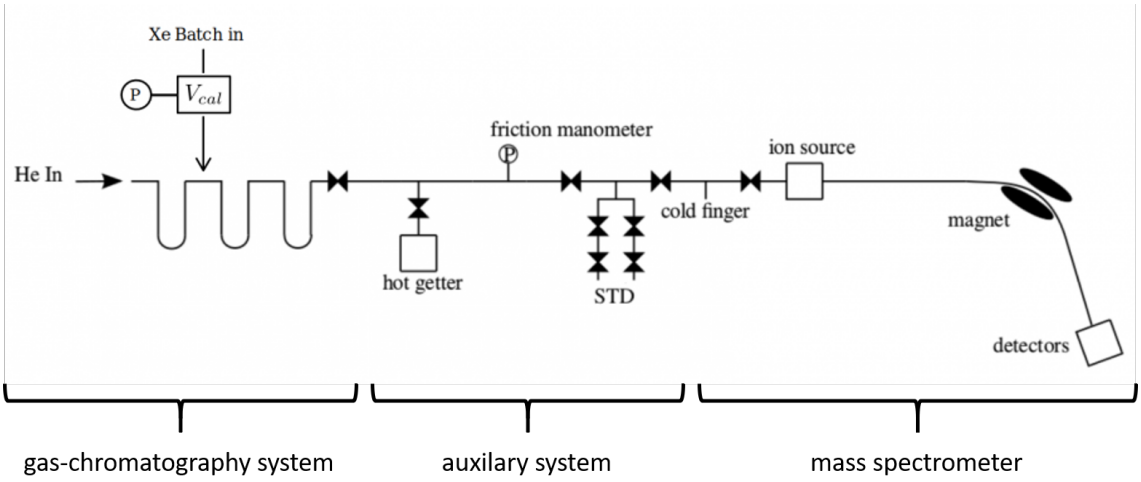

Figure 9: Simplified sketch of the total setup with the gas-chromatography system, the mass spectrometer and the connecting line, including the getter module and the standard calibration pipette volume STD [59].

The Mass Spectrometer

The RGMS set-up utilizes a customized sector field mass spectrometer consisting of the ion source, the mass analyzer, and the detector. A schematic view and a photograph is shown in Fig. 10.

Previous to analyzing krypton in xenon, it has mostly been used for applications in Earth and planetary science and has been optimized for the detection of chemically inert substances like noble gases. It has been shown to be able to detect amounts of natural krypton down to 10^{-13} ccmSTP, where *ccmSTP* denotes the volume at standard temperature and pressure [62].

For a measurement, the gas sample is transferred to a cold finger via cryogenic pumping. The cold finger is separated from the spectrometer volume by a valve (shown in the left part of the mass spectrometer section in Fig. 9). After reheating the cold finger and opening the connecting valve, the gas distributes in the entire volume of the ion source, the mass analyzer, and the detector. Ionization, acceleration and focusing take place in the ion source of the mass spectrometer.

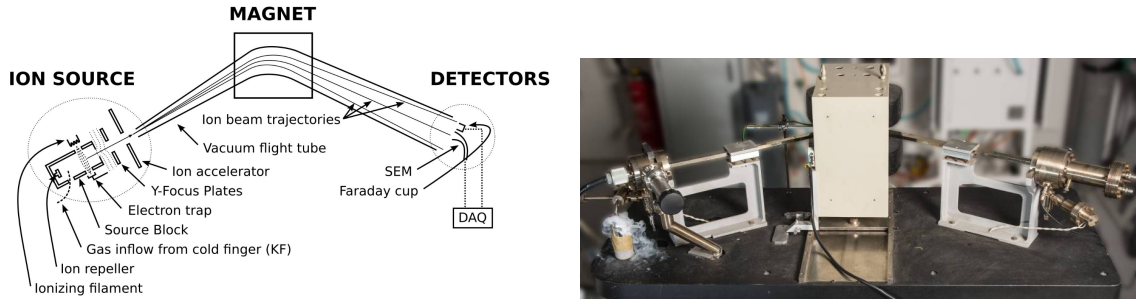

Figure 10: Schematic drawing (left) and photograph (right) of the mass spectrometer showing the mechanism of ionization in the source, the deflection of the ion trajectories and the two detection possibilities.

Electrons are emitted from a hot filament and accelerated by an electric field, ionizing the sample gas molecules along their way. The produced ions are extracted from the source by an applied high voltage and focused by two focal plates into the vacuum flight tubes. Mass separation is achieved by varying the approximately homogeneous dipole-field of the magnet, which deflects the ion beam trajectories depending on the ion mass. The ions are detected by a secondary electron multiplier (SEM) in case of a small signal ($<10^5$ ions/sec) or alternatively by a Faraday cup (not used in this work) in case of stronger signals. A SEM is a bent vacuum-tube coated with a so-called secondary emissive material. An incoming charged particle induces the emission of several electrons, which are accelerated by the electric potential inside the SEM and induce further secondary emission of electrons when hitting the walls. The resulting shower of electrons is collected by a metal anode at the end of the tube, where the amplified signal is finally measured. In a Faraday cup, the ions serve as moving charge carriers in vacuum. By measuring the electrical current generated by the ions, the number of ions is accessed.

The Gas-Chromatographic Setup

For optimal operating conditions, an ultra-high vacuum (UHV) with a residual pressure smaller than 10^{-6} mbar is required. Otherwise, the ion mean free path gets too small due to collisions with gas molecules and defined ion deflections in the applied magnetic field get impaired [63]. However, a xenon sample size of about 1 ccmSTP is required, since samples are expected to contain only trace amounts of krypton in the order of ppt or ppq and the sensitivity of the mass spectrometer is in the order of 10^{-13} ccmSTP. A sample size of about 1 ccmSTP is however in contradiction to the necessary vacuum conditions. Thus, a pre-separation of the krypton from the bulk xenon is mandatory. This separation is achieved by the cryogenic gas-chromatography system (developed in [58]).
The krypton-xenon separation by cryogenic gas-chromatography is performed with the set-up shown in Fig. 11. The underlying principle utilizes the different adsorption strength of krypton and xenon in an adsorbent filled column. This leads to a different breakthrough time, effectively separating the two components. In the following,

the overall separation procedure is described. The basics of gas chromatography are explained in Sec. 6.2.3, where different adsorbents are tested to optimize the separation process presented in this section.

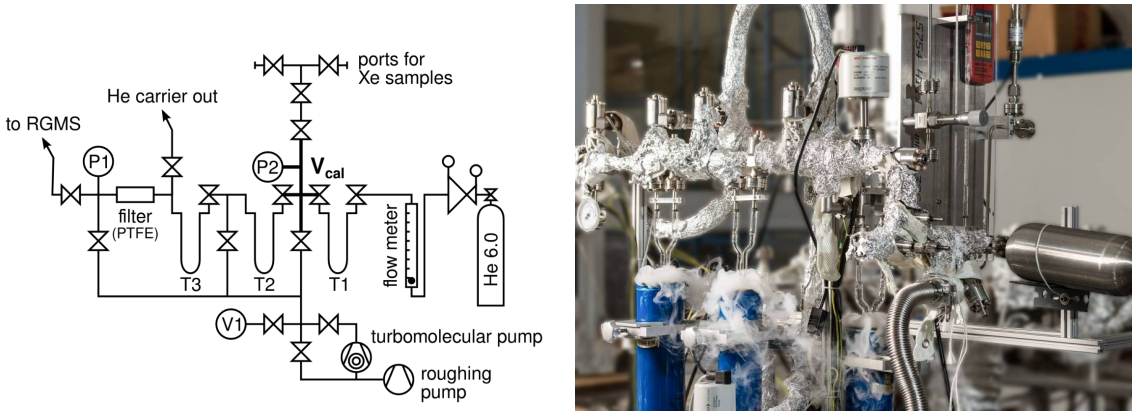

Figure 11: Schematic drawing (Left) and photograph (Right) of the cryogenic gas-chromatographic set-up. The three adsorbent filled columns are used for He-carrier gas cleaning, Kr-Xe separation and krypton collection. The system is equipped with a capacitive pressure gauge (P2) to determine the sample size [59, 61].

Grade 6.0 helium is used as carrier gas during the separation process, to push the sample gas through the adsorption column. To reach sub-ppt sensitivity, the krypton concentration in the helium has to be at least at the ppq level to avoid krypton contaminations in the carrier gas. Therefore, the helium is further purified by passing it through an adsorbent filled column (T1: 10 mm inner diameter, 8.18 g Carbosieve S-III by Supelco Analytical [58]) at liquid nitrogen (LN_2) temperature, where krypton traces get trapped efficiently ($^{nat}Kr/^{pur}He < 0.012$ ppq [59]) and the residual impurity can safely be neglected.
A sample pipette (Fig. 12) is mounted at the sample port from where a batch of xenon can be expanded into the calibration volume V_{cal}. The batch size is determined by its pressure in V_{cal} at room temperature, measured by a capacitance pressure gauge (P2). After the sample size is determined, the sample is frozen to a second adsorbent filled column T2 (6 mm inner diameter, 0.65 g Chromosorb 102 by Johns Manville [58]), which is at LN_2 temperature. Then the chromatographic process is started by increasing the temperature of the column by immersing it into a cooled ethanol bath with a fixed temperature of $-90\,°C$ while flushing with 40 ml/min of helium carrier gas to push the sample gas mixture through the column. Due to the different interaction strength with the adsorbent, krypton and xenon get macroscopically separated and exit the column at different times. Krypton passes the column faster than xenon and is collected at a third adsorbent filled column T3 (identical to T2) at LN2 temperature, which is closed by an interconnecting valve before the xenon can pass the second column T2. For more details on the separation power see [59]. By heating up T3 afterward, the krypton is released and transferred to the mass spectrometer by cryogenic pumping to the cold finger (Fig. 9). The acceptance of the

chromatographic procedure for krypton was determined in [58] as a_{Kr}=0.97 ± 0.02. To satisfy UHV conditions of $\sim 10^{-9}$ mbar, all parts of the set-up are selected for high purity standards. Only stainless steel tubes, copper sealed flanges, and fully metal sealed valves are used. The micro-packed adsorbent filled columns are made of borosilicate glass with special glass to metal seals and a PTFE particle filter prevents dust of the adsorber materials from contaminating the spectrometer [58]. The ultra-high vacuum is realized by a pumping system consisting of standard turbo molecular pumps, roughly pumps as well as partially oil-free vacuum pumps to avoid contamination of the adsorbents with hydrocarbons.

Measurement Procedure

In a standard procedure measurement, xenon samples are filled into so-called sample pipettes. They consist of four fully metal sealed valves welded together, creating three sub-volumes (see Fig. 12). Before filling the sample into the pipette, it is baked moderately (∼100 °C) and pumped for a few days in order to remove residual krypton contaminations. To analyze the sample, the pipette is mounted to the RGMS's input port and the connecting volume is baked and pumped for several days, again to avoid contaminations from the air.

Figure 12: Xenon sample pipette. The port on the right is connected to the RGMS input port, the port on the left is used for baking, pumping and sample filling.

The measurement procedure begins by extracting xenon from the pipette's first volume. Each volume of a pipette is measured separately to identify possible leaks within the pipette. The extracted sample from one volume can be divided further into small batches by several smaller volumes between the pipette and V_{cal}. Each of these batches is then analyzed individually to have multiple measurements of each pipette volume (called try). The batch used for the measurement is then expanded to the calibration volume V_{cal}. The remaining gas is stored inside the volumes between V_{cal} and the sample pipette for following measurements.
The batch in V_{cal} is then transferred to T2 (see Fig. 11) and the chromatographic process as described above is started. The standard acceptance window (closing of

the valve between T2 and T3 to cut off the bulk xenon) is 15 min. After pumping the remaining helium carrier gas from T3, which is still immersed in LN2 to keep krypton trapped, it is heated up again. Subsequently, the gas is transferred to the cold finger of the mass spectrometer by cryogenic pumping for 40 minutes (During this time the main spectrometer parts are still evacuated). This involves opening a valve to an additional high-temperature getter module to remove non-inert impurities by chemically binding them. These impurities can pass the chromatographic process due to similar retention times to that of krypton or can be released by Chromosorb or by any other surface previously exposed to air. Thereby, the pressure is monitored to make sure that the chromatographic separation did not fail and that potential leaks are detected before letting the sample gas into the spectrometer.
After that, the valve between the line and the cold finger is closed and the cold finger is warmed up to room temperature. At the same time evacuation of the spectrometer is stopped and data acquisition starts. The background evolution for the considered isotopes is recorded for about 20 min. Due to outgassing of residual noble gases from the spectrometer walls, a slight increase in the observed background can be seen during this time. At time t_0, referred to as gas-inlet, the valve between the cold finger and the spectrometer is opened and the gas distributes into the spectrometer. After gas-inlet, the magnetic field is set to the investigated mass and kept constant for a few seconds until the signal is stable. The signal strength is measured by counting the number of pulses of the SEM above a certain threshold for 1 s. Several data points (8-12) are taken for constant field settings to improve statistics. To take the dark count rate of the SEM into account, the signal strength left and right of the peak of the investigated isotope is determined. The final value for the signal strength of an isotope at the time of measurement is then calculated by averaging the data points taken at the literature mass and subtracting the dark count rate average. The baseline-corrected value marks the signal strength for the respective isotope at the time of measurement. In Sec. 4.2.3 the signal evolution is explained in more detail.
In the standard measurement procedure, several isotopes are investigated. A loop is applied, running over the masses of the considered isotope. It lasts approximately one minute for each pass, executing the process described above for each isotope. This results in one data point per isotope per minute. Usually, ^{36}Ar, ^{84}Kr and ^{86}Kr are measured. ^{84}Kr and ^{86}Kr are used for the computation of the krypton amount in a sample, while ^{36}Ar is used to confirm the ratios between the different elements, which have to match their natural abundances. Additionally, ^{129}Xe** (double ionized) is counted at the end of a measurement. The double ionized xenon is used instead of the singly ionized one since it has a considerably lower count rate which protects the SEM and preserves its sensitivity. The xenon measurement is used to monitor the chromatographic separation process. If the separation of krypton and xenon works perfectly, only krypton should be transferred from T3 to the cold finger, while xenon is still trapped in T2. Therefore, only a minimal amount of xenon should be present in the spectrometer, originating e.g. from outgassing in the set-up or a non-perfect separation.

After a measurement is performed and during idle, the whole set-up is pumped. Also, the adsorbent filled columns are heated to remove residual gas and to avoid adsorption of gas originating from background into the column.
Additional to the standard procedure measurement, several more measurement modes are used. First and foremost the set-up needs to be calibrated. A gas standard is available, which is composed of the noble gases argon, krypton and xenon that are filled to a metal sealed container of a few liters volume. To a good approximation, a constant fraction of the gas standard (STD) can be extracted by expanding the gas in a much smaller volume ($\sim$0.2 cm^3), which is separated by fully metal sealed valves. The amount of krypton in one standard pipette was calibrated in [58] to be 3.9×10^{-11} cm^3($\pm$16.5%)(xenon $\sim 5 \times 10^{-11}$ cm^3, argon $\sim 4 \times 10^{-8}$ cm^3). The STD is used to calibrate the magnetic field by performing a scan across the full field and identifying the peaks corresponding to the occurring isotopes. The calibration mixture is furthermore used for an absolute calibration of the response of the mass spectrometer to a quantified amount of gas. Before a sample measurement is performed, the STD is frozen to the cold finger and then expanded to the spectrometer. The response of the spectrometer to the known gas amount is recorded. This is called *standard pipette measurement* and is usually performed in parallel to the chromatographic separation process of the sample. Moreover, regularly *blank measurements* are performed. In a *blank measurement* the chromatographic procedure (identical to a normal measurement), but without a xenon batch introduced to V_{cal}, is performed. This is done to estimate the remaining krypton impurities resulting from tiny air leaks outgassing from the GC system and the connecting line and the residual contamination of the helium carrier gas. This background is later subtracted from the sample measurement (see Sec. 4.3). To remove the residual gas as best as possible, the complete set-up is occasionally baked-out with heating covers, while pumping the desorbed gas away. The stainless steel and glass part of the system is bake-able to above 300 °C, however, adsorbent materials and PTFE filter only withstand temperatures up to 150 °C, setting the upper limit on the temperature during bake-out. Some parts of the GC and connecting lines are heated permanently to minimize the adsorption of residual gas at these parts.

4.2.3 Signal

Expected Signal

In the analysis, one is interested in the amount of gas introduced to the mass spectrometer. As mentioned before a slight increase in the count rate can be seen during the background measurement. Opening the connecting valve and introducing the sample to the spectrometer, results in an immediate increase of the count rate. After that, implanting of the ions into the spectrometer walls leads to a slowly decreasing signal. Fig. 13 shows the expected signal evolution.
To evaluate the krypton amount, the pedestal between pre- and post-gas-inlet has to be calculated. The time dependence of the two regions (count rate of the background and count rate of the signal) are both fitted separately and then extrapolated to t_0,

the time of gas inlet. The size of the pedestal at t_0, as seen in Fig. 13, quantifies the amount of gas that was introduced by the sample.
This fit is performed for each respective isotope considered in the measurement loop. In this way a pedestal value with its respective error from the fit for each isotope is obtained.

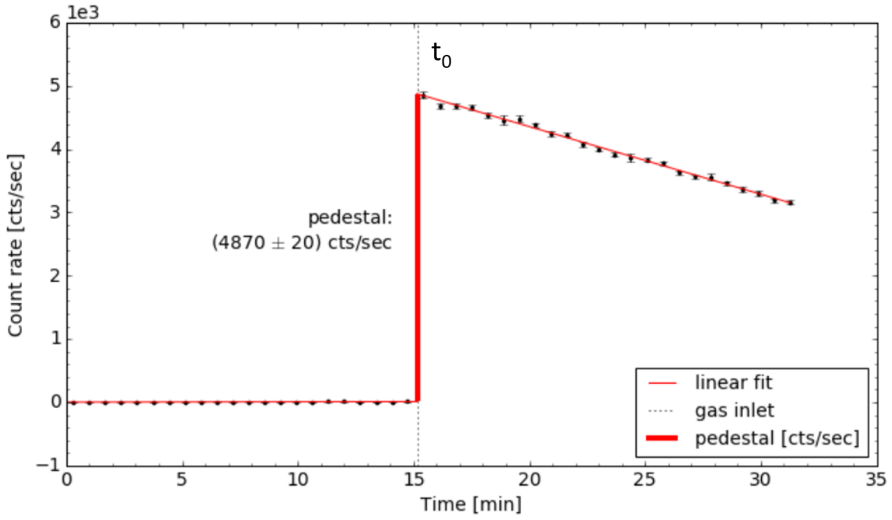

Figure 13: Exemplary time evolution of the expected ^{84}Kr signal. At t_0 the gas is introduced to the spectrometer and the pedestal is quantified by linear fits of the background and signal region.

Observed Signal

During the work of [60] a non-linear behavior of the count rate during data taking was observed. Instead of a linear decrease after gas-inlet, the signal starts to grow non-linearly until reaching a certain maximum and eventually decreases again. This signal evolution, in the following referred to as grow-in effect, can be seen in Fig. 14. A thorough analysis was performed in [60]. A possible explanation was that the grow-in structure could be the result of a memory effect, where ions that were deeply implanted into the SEM surface and the spectrometer walls are knocked out again by collisions with other ions and thereby leading to a growing signal evolution, while on the other hand adsorption of the ions into the spectrometer walls lead to the aforementioned slowly decreasing signal. The krypton amount then corresponds to the actual jump in the SEM signal at gas-inlet. An empirical fit function was introduced to implement this into the fitting procedure.

$$f(t) = (mt + b) + y_0 \cdot \left(1 - e^{-l(t-t_0)}\right) \tag{1}$$

The first term describes the linear decline of the count rate due to the adsorption of the ions. It is superimposed by the second term that models the limited exponential

growth of the signal resulting from ions being knocked out, with the limit of y_0, the growth constant l and the time of gas-inlet t_0. The pedestal can then be quantified as usual by comparing the fitted count rates for the two fit regimes before and after gas-inlet.

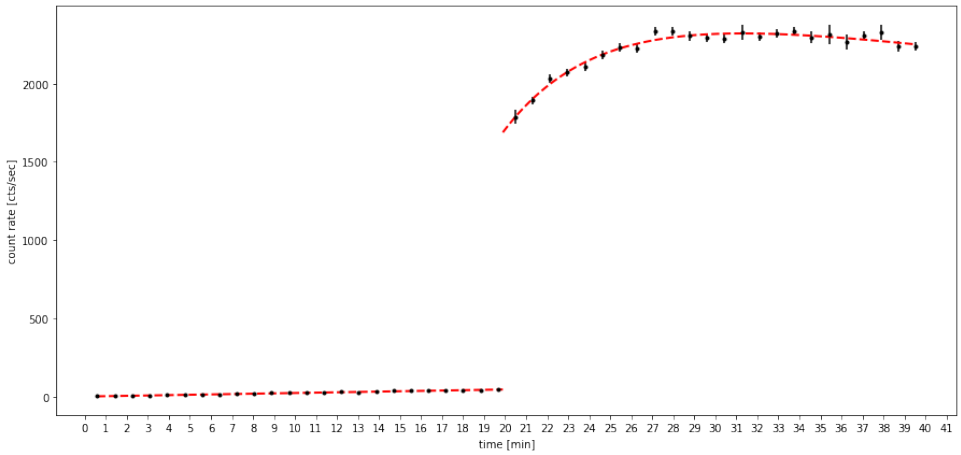

Figure 14: Exemplary time evolution of the observed ^{84}Kr signal with exponential grow-in effect after gas-inlet and dedicated fitting function.

4.3 Calculation of the Krypton Impurity Level

The krypton impurity level *KIL* is calculated by dividing the amount of natural krypton in the xenon sample by the size of the xenon sample. This is done the following way:

$$KIL = {}^{\text{nat}}Kr/Xe = \frac{< Kr_i - B_i > \cdot a_{Kr}^{-1}}{Xe} \tag{2}$$

, where

- $Kr_i = \dfrac{ped_i^{batch}}{ped_i^{STD}} \cdot Kr^{STD}$, $B_i = \dfrac{ped_i^{blank}}{ped_i^{STD}} \cdot Kr^{STD}$

  with Kr^{STD} = amount of Kr in standard
  ped_i^x = pedestal of measurement type x
  i = isotope under consideration

- $Xe = \dfrac{p}{p_0} \cdot V_{cal} \cdot \dfrac{T_0}{T}$ (Amount of gas in sample)

$$
\text{with} \quad
\begin{array}{ll}
p = \text{pressure in } V_{cal} \ , & V_{cal} = (112 \pm 0.5) \text{ cm}^3 \\
p_0 = 1000 \text{ mbar} \ , & \Delta p = 2.3\% \\
T_0 = (273 \pm 2) \text{ K} \ , & T = (294 \pm 3) \text{ K} \\
a_{Kr} = 0.97 \pm 0.02 &
\end{array}
$$

The size of the xenon sample Xe is obtained by transforming the measured pressure p in the known volume V_{cal}, while assuming room temperature, into a sample size in standard conditions (ccmSTP).
To derive the natural krypton amount $^{\text{nat}}Kr$, several calculation steps are necessary: First, the individual measured ^{84}Kr and ^{86}Kr pedestals of the sample ped_i^{batch} (isotope denoted by i) are scaled to the response of the SEM to the calibration pipette measurement ped_i^{STD} resulting in Kr_i.
The same calculation is done for the *blank measurements* ped_i^{blank}. The resulting blank amounts are usually averaged over several such measurements over a period of time with similar operating conditions to obtain B_i.
Next, the individual blank value of ^{84}Kr and ^{86}Kr are subtracted from its respective calibrated sample measurement $Kr_i - B_i$ and the weighted average $< ... >$ of the two isotopes is taken. Last, the chromatographic acceptance parameter a_{Kr} is incorporated to obtain the amount of natural krypton in the sample and consequently the krypton impurity level.
The error calculation of the KIL is divided into two parts. First, there is the uncorrelated error. It results from the statistical uncertainty of the data points and consequently from the uncertainty of the fit of the pedestal.
Second, there is the correlated error. It results from systematic uncertainty arising from e.g. variations in performing the chromatographic separation or variations in the electrical fields of the ion optics. This also includes the uncertainty of the krypton amount in the calibration gas. Since the uncertainty of the calibration gas significantly dominates the uncertainty budget, the correlated error is simply calculated by multiplying the obtained KIL by the uncertainty of the calibration gas. The result of a measurement is then displayed the following:
KIL $\pm$ *uncorrelated error* $\pm$ *correlated error*
Since for each sample pipette several measurements are performed, the weighted average using the uncorrelated error is taken (if larger deviations arise, which can be explained, e.g. by a leak in a pipette volume, these measurements are discarded). This way a single value for a certain pipette is obtained.

5 Evolution of the Krypton Concentration in XENON1T

5.1 Motivation

Since XENON1T is an ultra-low background detector, a good understanding of the sources and features of background radiation is crucial in order to be able to detect a rate excess that might be induced by a dark matter particle. This includes having a precise knowledge about the detector's background conditions and having a complete background model.
In the case for the internal background component ^{85}Kr (see Sec. 3.3.1), the amount of krypton in xenon is monitored by the RGMS (see Sec. 4.1). Xenon sample pipettes were drawn regularly from the XENON1T detector to monitor the timely evolution of the krypton concentration in the detector. This is done during science runs, but also and especially when operations at the detector were performed, which could have led e.g. to an exposure to air, increasing the krypton level. The obtained evolution of the krypton concentration is also of great importance in regard to annual modulation studies, where a dark matter detection could be possible by the expected varying signal over the year (see Sec. 2.4.1) [64].
In this chapter, a re-evaluation of gas sample measurements, performed with the RGMS, is described. The investigated samples originate from XENON1T, in particular from January 2018 until the detector was decommissioned. The reason for a reconsidered analysis of these samples is a change of the signal shape of the RGMS. The RGMS had a longer period of downtime due to problems in the chromatographic procedure and the krypton in xenon analysis was not possible in a consistent way. During resolving this issue also some hardware in the spectrometer was exchanged, in particular the SEM and some parts of the ionization source. After these problems were solved, the krypton in xenon analysis was running smoothly again, but the signal of the RGMS had new and not understood features. The aforementioned samples were measured with this new arisen signal evolution. A new fitting procedure to extract the gas amount from the signal evolution and a different thorough error treatment was needed. XENON1T samples earlier than January 2018 were measured and analyzed as part of [60] with the methods described in Sec. 4.2.3 and Sec. 4.3.

5.2 Signal Behavior

In Sec. 4.2.3 the expected signal evolution and the measured grow-in structure was described. XENON1T samples until January 2018 had this type of signal evolution. The measurements analyzed in this work have the type of signal evolution exemplary shown in Fig. 15 for calibration measurements and Fig. 16 for sample and blank measurements. The signal of the background measurement before gas-inlet did not change and consistently maintains a small linear increase.
The response of the RGMS to a calibration measurement still shows the grow-in structure, which arose before, but here the turn into the linear decrease is not smooth and shows a bend. The previously used grow-in fitting function eq. 1 does

not describe this bend and is also not able to represent the nearly linear decrease afterward properly.

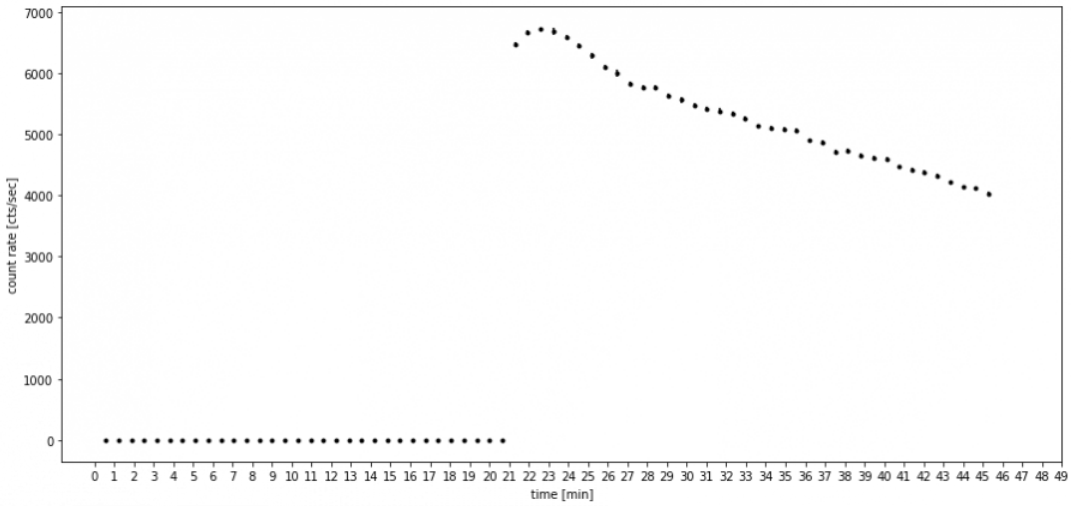

Figure 15: Exemplary signal evolution of a calibration measurement. The signal after gas-inlet shows a grow-in structure at the beginning, which turns not smoothly into a linear decrease.

The response of the RGMS to a signal or blank measurement does not show the grow-in structure anymore. Instead, a so-called hill-structure is apparent after gas-inlet, which is a sharp linear or exponential decrease after gas-inlet, turning with a bend into a less linear decrease. This is again not described by the previously used fitting function.

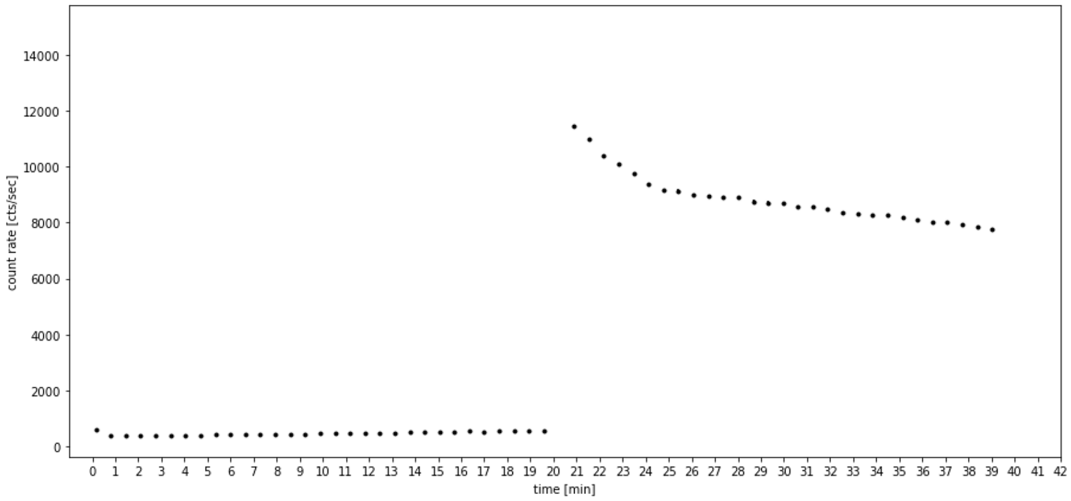

Figure 16: Exemplary signal evolution of a sample measurement. The signal after gas-inlet shows a hill-structure at the beginning, which turns not smoothly into a linear decrease.

5.3 Analysis

5.3.1 General Observation

For all measurement types two regions seem to appear, a grow-in/hill part at the beginning and a linear decreasing part at the end, which are not going smoothly into each other.
The arising problem is that it is not clear which data points lead to the correct pedestal. On one hand, the early data points after gas-inlet could describe the true pedestal with the introduced gas amount and afterward some effect changes the signal evolution into the observed bend. On the other hand, some background or detector effect could be responsible for the increase of the early data points and the corrected pedestal is obtained by extrapolating the later data points to the time of gas-inlet and extracting the gas amount. Consequently, the pedestal of the early few data points is most of the time significantly higher than the extrapolated pedestal from the later data points.

5.3.2 Analysis Procedure

At this point, it is not possible to decide on which data points to put more trust in. Nevertheless, a way to proceed is necessary to get reasonable results for the krypton in xenon analysis. For this reason following analysis procedure is performed to obtain the pedestals of the calibration as well of the blank and sample measurements. In this approach, it was decided to be most conservative to take the uncertainty of the correct pedestal into account.
The background region before the gas-inlet is fitted as before, here nothing has changed. For the region after the gas-inlet two fits are carried out.

1. Only the early few data points until the bend are used, while the later ones are discarded, called *front fit*. The following fitting function used:

$$f(t) = y_0 \cdot (1 - e^{-l \cdot t}) + (m \cdot t + b) \tag{3}$$

   This is the usual grow-in function as described in Sec. 4.2.3. The use of this function is continued because it can describe the grow-in structure of the early few data points of the calibration measurements, but also the linear or exponential decrease of the early data points of sample and blank measurements by either taking the exponential or linear part of the summed function while taking the other part to zero.

2. The early few data points are discarded and only the later data points constituting the linear decreasing part are fitted with a linear fit function.This is called *back fit*. The fit is then extrapolated to the time of gas-inlet t_0.

The background fit pre-gas-inlet and these two fits are performed for each measurement (calibration, blank or sample) and the pedestal is extracted as described in

Sec. 4.2.3. The fitting procedure is illustrated in Fig. 17 for a sample measurement (top) and for a calibration pipette measurement (bottom). The blue line represents the front fit with the blue band indicating the fitting region, while the green line and band represent the back fit, respectively. Depending on the individual measurement, the fitting regions are not adjacent.

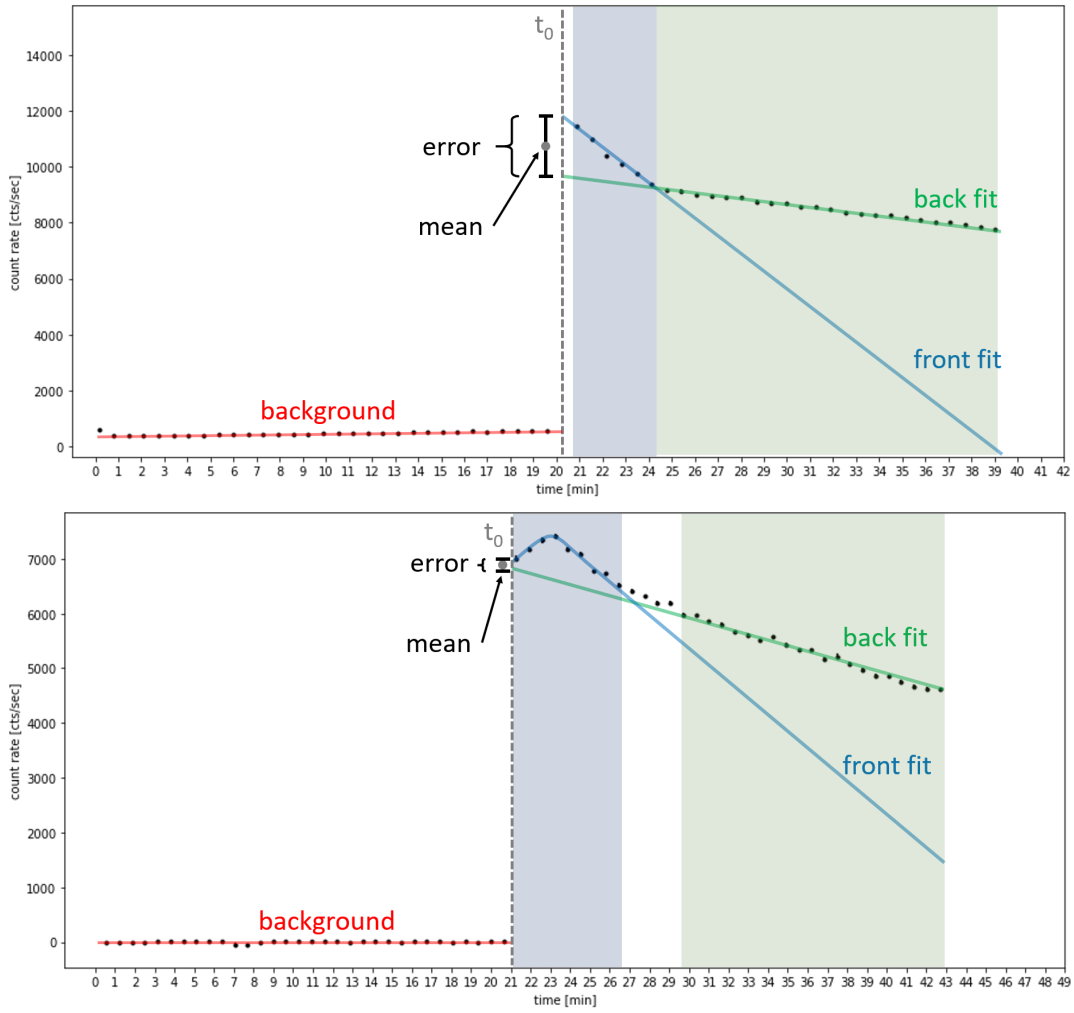

Figure 17: Illustration of the fitting procedure of a sample measurement with a hill structure (top) and a calibration pipette measurement with a grow-in structure (bottom). The blue line represents the front fit with the blue band indicating the fitting region, while the green line and band represent the back fit, respectively. In most sample measurements the transition between the two fitting regions is smooth, while for calibration pipette measurements the two fitting regions are most of the time not adjacent. The pedestal is calculated by taking the average of the pedestals resulting from the two fits and increasing the error to include both individual pedestal values.

Since both pedestals could describe the introduced gas amount, the results of the two fits are averaged. To be most conservative, the statistical error is discarded

and the error on the mean value is increased to contain each individual pedestal of the fits as shown in the plots. The deviation between the two fits varies in size for different measurements but is strictly larger than the statistical error of the fits. Therefore, the pedestal value has no statistical, but a systematic error, which will be of importance in the error calculation later on.

5.3.3 Calibration Evaluation

First, the calibration measurements are evaluated. The reason for the appearance of the grow-in structure only for the calibration measurements is not yet clear. An explanation could be related to the general gas amount. The calibration pipette measurement has a higher gas amount and consequently a higher count rate than a sample measurement (see Sec. 4.2.2). Furthermore, it could be connected to the individual gas concentration in the pipette. As seen on page 27, the argon concentration is about 3 orders of magnitude higher in comparison to krypton and xenon. ^{36}Ar measurements (not shown) only show a tiny grow-in structure or none at all. Another possibility is, therefore, an effect regarding a specific isotope or element like argon. Dedicated measurements with varying amounts of calibration gas are going to be performed to investigate this hypothesis further (not part of this thesis).

Calibration Pipette Time Evolution

After fitting of the calibration measurements and the calculation of the average and its error with the procedure described above, the time evolution of the calibration for ^{84}Kr and ^{86}Kr is examined (see Fig. 18). The plot serves only as an illustration for the investigation of the evolution of the SEM response over time. For a sample measurement, the response of the SEM is acquired beforehand and used individually for this specific sample measurement.
The time evolution for ^{84}Kr and ^{86}Kr agree, so one can conclude that there is no effect regarding a specific krypton isotope. The deviations ($\sim$10%) between the two fits resulting in different pedestals are incorporated in the error bars. The grey lines indicate operations performed on the RGMS, which changed the sensitivity of the SEM. Before heating, the response of the RGMS dropped significantly, which was due to an accidental exposure of the spectrometer to a larger amount of xenon. To remove the residuals of xenon and to restore the sensitivity of the SEM, the set-up was baked. No sample measurement was performed in the region of lower sensitivity. The sensitivity increases after the heating period and then slowly decreases due to aging of the SEM. To increase the sensitivity again, the voltage of the SEM was raised.

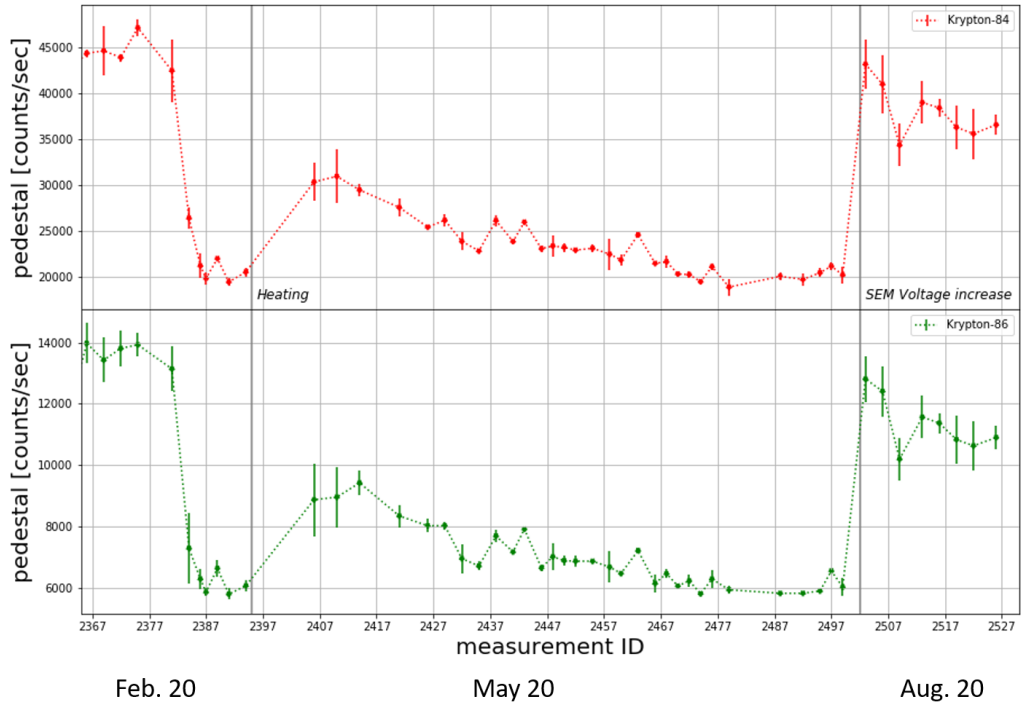

Figure 18: Illustration of the time evolution of calibration measurements for ^{84}Kr (top) and ^{86}Kr (bottom) obtained with the applied fitting procedure. Operations explaining larger jumps in the evolution are indicated. The size of the errorbars depends on the difference between the two fits. The response of the SEM is acquired beforehand and used individually for a sample measurement. The dates show an approximate correspondence to the measurement ids.

5.3.4 Blank Evaluation

Next, the blank measurements are investigated. Here also a small hill-structure is apparent. Due to the low count rate and the associated varying signal of the blank measurement, it is not pronounced for some measurements. The fits heavily depend on the fit details, which results in some deviation between the two fits. Nonetheless, this is not worrisome for this analysis as the blank value barely makes a difference, which will be seen later on in the krypton impurity level calculation.
Besides the standard blank measurement, also diagnostic blanks were performed to identify and fix leaks and other problems. They were not considered in the blank evaluation discussed here. In these so-called *grow-in blanks*, the investigated volumes are not pumped for some time to accumulate residual gas before the measurement is performed. Instead of a straight decreasing "hill"-structure as for standard blank measurements, an exponential decrease is apparent.

Blank Time Evolution

The evaluated blank measurements are shown in Fig. 19. Since blank measurements are performed irregularly, a blank value that is valid in a certain time period is needed. In regions where blank values agree, the mean of the maximal deviations within the errors is taken (blue line in Fig. 19). The error of the mean value is increased to include these maximal deviations of individual blank values (blue band in Fig. 19). This leads to two different regions with their respective blank values shown below.

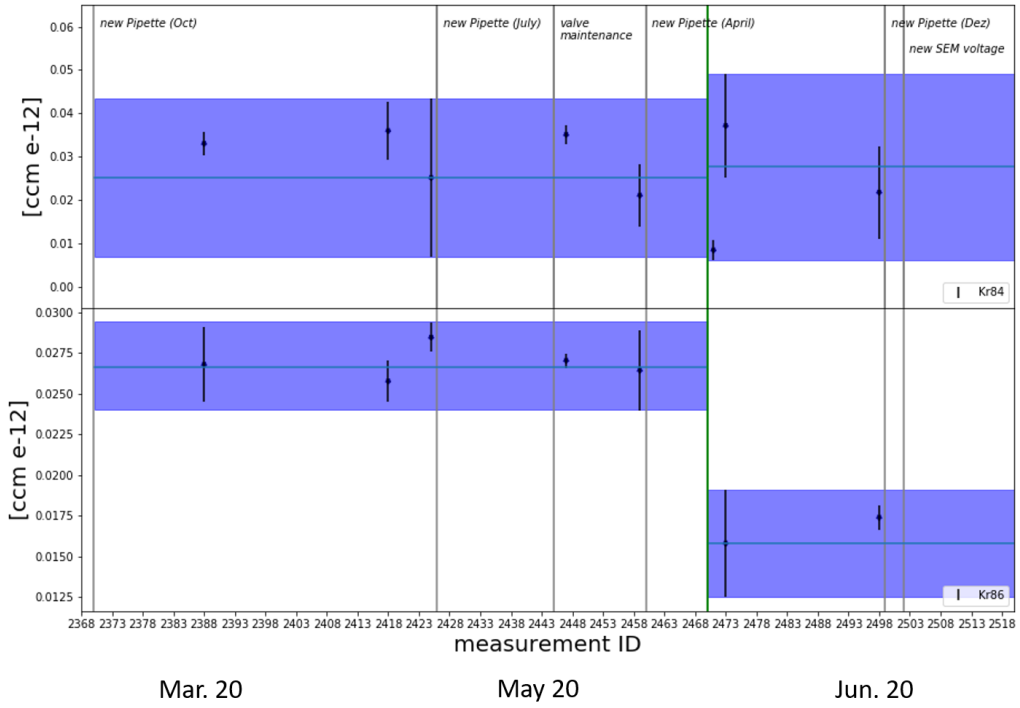

Figure 19: Time evolution of blank measurements for ^{84}Kr (top) and ^{86}Kr (bottom). Operations on the RGMS and sample pipette exchanges are indicated. In regions, where different blank values agree, the mean of the maximal deviations within the errors is taken (blue line) and the error is increased to take these possible deviations into account (blue band). The green line then indicates the change between the two blank value regions. The dates show an approximate correspondence to the measurement ids.

Valid blank values [10^{-12}cm^3]:

- 0.0251 ± 0.0183 for ^{84}Kr and 0.0266 ± 0.0027 for ^{86}Kr until Id 2470
- 0.0276 ± 0.0215 for ^{84}Kr and 0.0158 ± 0.0033 for ^{86}Kr after Id 2470

5.3.5 Sample Evaluation

Last, the sample measurements are evaluated. For the sample measurements, the same hill-structure as for the chromatographic blank measurements appears, but more consistently i.e. all measurements show this feature, but in various strength. The front fit is either linear or slightly exponentially decreasing. Nevertheless, the front fit is consistently above the back fit.
Several checks are performed to investigate the hill-structure and the extend of the difference between the two fits. No correlation is found to the xenon amount remaining in the sample after separation (xenon scan after the measurement as described in Sec. 4.2.2). Also, the gas amount does not seem to influence the extent of the hill structure. A correlation of the bend to a certain time or a certain count rate is not perceptible. However, the higher the gas amount of the sample, the higher is the deviation between the two fits, but the residuals do not show a trend. Dedicated tests have to be performed to investigate the features of the signal evolution, which is outside of the scope of this thesis.

5.3.6 Calculation of the Krypton Impurity Level

After analyzing each measurement type and calculating a pedestal value with its respective error for all measurements, the krypton impurity level is then calculated the same way as described in Sec. 4.3. The only exception is, that not the weighted average, but just the average of the isotopes is taken. This is due to not having a statistical error but only a systematic error originating from the uncertainty of the true pedestal (see Sec. 5.3.2). This fact is also going to reflect in the error calculation of the krypton impurity level.
As indicated in Fig. 16 typical count rates of sample measurements are in the order of 200 cts/s to 12 000 cts/s, while blank measurement have count rates of ∼20 cts/s to 50 cts/s. Consequently, the deduction of the blank value does not have a large impact on the calculation of the krypton impurity level.
The error calculation is performed the following way: Since the statistical error was discarded, the error calculation as described in Sec. 4.3 with Gaussian error propagation is not applicable and the error format of $KIL \pm$ *uncorrelated error* $\pm$ *correlated error* is not possible. Instead, a systematic error on the pedestal values was used to incorporate the uncertainty of the true pedestal. To transfer this error to the krypton impurity level, the maximal error is applied. For each computation step, the maximal deviations (upwards (max) and downwards (min)) within the errors of the calculated value are computed and averaged.
As an example the error calculation of the calibration is given.

$$Kr = \frac{ped^{batch}}{ped^{STD}} \cdot Kr^{STD}$$

$$max = \frac{ped^{batch} + err\_ped^{batch}}{ped^{STD} - err\_ped^{STD}} \cdot Kr^{STD}$$

$$min = \frac{ped^{batch} - err\_ped^{batch}}{ped^{STD} + err\_ped^{STD}} \cdot Kr^{STD}$$

$$err\_Kr = \frac{(max - Kr) + (Kr - min)}{2}$$

This is done for the complete calculation and results in an error of the order of $\sim$ 20%.

5.4 Results

5.4.1 Explanation of drawn Pipettes

The pipettes evaluated within this thesis were drawn for the following reasons.

- **Pipette No.9 (January 2018) & Pipette No.3 (April 2018):**
  These two pipettes were taken to monitor the regular operation of the detector during a science run, acquiring dark matter data.

- **Pipette No.2 (July 2018):**
  In the time between the 29^{th} of May to the 16^{th} of June, a magnetic pump had to be exchanged. Since this was an operation in the gas circulation system, this pipette was drawn afterward.

- **Pipette No.8 (October 2018):**
  Additional new xenon was filled into the detector, which could have introduced a higher krypton amount into the system. Consequently, this pipette was drawn to monitor this operation. Since the science runs were finished and a distillation phase was planned, this pipette was also taken as reference level before the distillation.

- **Pipette No.10 (December 2018):**
  A distillation phase from 6^{th} of November to 10^{th} of December was performed. Afterward, this pipette was taken to obtain the performance of the distillation.

5.4.2 Calculated Krypton Impurity Level

The krypton impurity level and its error are calculated for all measurements regarding these pipettes. The results are shown in Tab. 1. The outcome of each pipette is shown individually. Additionally, for each pipette, the volume of the pipette and the number of measurement of the volume (try) is indicated, as described in Sec. 4.2.2. In the column showing the krypton impurity level results, the correlated error related to the uncertainty of the true signal is indicated by *cor sig*, the correlated error related to the uncertainty of the krypton amount in the calibration gas is indicated by *cor cal*. For each pipette, the average of the individual measurements is taken and written in bold. Also, the total error is calculated by adding the two errors quadratically.

It is also apparent that measurements of certain volumes/tries are not shown. They are discarded for one of the following reasons.

- The volume of the pipette was leaky, resulting in an inconsistent krypton concentration in comparison to the other two.
- A tiny leak in the volumes where samples are divided into small batches and stored between measurements (see Sec. 4.2.2). This leak is reflected by an increase of the krypton concentration for each try depending on the storage time.
- An error in the measurement procedure occurred.
- Some pipettes were already measured in the past, where the chromatographic procedure was not working properly.

Pipette	ID	Volume/Try	Date	Xe [ccm]	Kr/Xe [ppt]
9 (26.Jan)	2427	3/1	20.04.20	1.512 ± 0.022	0.68 ± 0.15 cor sig ± 0.11 cor cal
9 (26.Jan)	2436	3/4	30.04.20	1.491 ± 0.022	0.68 ± 0.13 cor sig ± 0.10 cor cal
					0.68 ± 0.14 cor sig ± 0.11 cor cal
					0.68 ± 0.18 tot
3 (19. April)	2477	2/1	30.06.20	1.200 ± 0.017	0.86 ± 0.27 cor sig ± 0.13 cor cal
3 (19. April)	2480	2/2	02.07.20	0.986 ± 0.014	0.91 ± 0.19 cor sig ± 0.14 cor cal
3 (19. April)	2489	3/1	06.07.20	1.416 ± 0.021	*2.29 ± 0.31 cor sig ± 0.35 cor cal*
3 (19. April)	2493	3/2	08.07.20	1.362 ± 0.020	*2.16 ± 0.35 cor sig ± 0.33 cor cal*
					0.89 ± 0.23 cor sig ± 0.14 cor cal
					0.89 ± 0.27 tot
2 (9.July)	2453	1/1	29.05.20	1.491 ± 0.022	2.02 ± 0.40 cor sig ± 0.31 cor cal
2 (9.July)	2456	1/2	01.06.20	1.648 ± 0.024	2.21 ± 0.42 cor sig ± 0.34 cor cal
2 (9.July)	2461	2/1	05.06.20	1.560 ± 0.023	1.97 ± 0.38 cor sig ± 0.30 cor cal
2 (9.July)	2464	2/2	09.06.20	1.243 ± 0.018	2.14 ± 0.43 cor sig ± 0.33 cor cal
					2.09 ± 0.41 cor sig ± 0.32 cor cal
					2.09 ± 0.52 tot

Pipette	ID	Volume/Try	Date	Xe [ccm]	Kr/Xe [ppt]
8 (18. Oct)	2370	3/1	24.02.20	1.263 ± 0.018	1.88 ± 0.55 cor sig ± 0.29 cor cal
8 (18. Oct)	2379	3/4	02.03.20	1.166 ± 0.017	1.84 ± 0.43 cor sig ± 0.28 cor cal
					1.86 ± 0.49 cor sig ± 0.29 cor cal
					1.86 ± 0.57 tot
10 (10. Dec)	2500	1/1	21.07.20	1.570 ± 0.020	0.063 ± 0.019 cor sig ± 0.010 cor cal
10 (10. Dec)	2504	1/2	23.07.20	1.610 ± 0.020	0.091 ± 0.020 cor sig ± 0.014 cor cal
10 (10. Dec)	2511	2/2	30.07.20	0.950 ± 0.010	0.116 ± 0.038 cor sig ± 0.018 cor cal
10 (10. Dec)	2514	3/1	10.08.20	1.410 ± 0.020	0.044 ± 0.020 cor sig ± 0.007 cor cal
10 (10. Dec)	2517	3/2	12.08.20	1.120 ± 0.020	0.131 ± 0.028 cor sig ± 0.020 cor cal
10 (10. Dec)	2520	3/3	18.08.20	1.770 ± 0.030	0.233 ± 0.063 cor sig ± 0.036 cor cal
					0.193 upper limit @ 90% C.L.
					0.054 ± 0.020 cor sig ± 0.009 cor cal
					0.054 ± 0.021 tot

Table 1: Krypton in xenon concentration for the samples evaluated with the procedure described in this thesis. A sample was drawn from XENON1T and filled into pipettes during science runs as well as and especially after detector operations to monitor the krypton impurity level. A pipette consists of four fully metal sealed valves welded together, creating three sub-volumes. Each volume of a pipette is measured individually and separated into several small batches. Therefore, for each pipette volume, multiple measurements result, called tries. For each pipette, a final value is obtained by averaging the different measurements. For the December pipette, only an upper limit can be given, resulting in the lowest krypton concentration ever measured in a running detector.

For the pipette taken in April (No.3) the measurements of the 3^{rd} volume are excluded from the final value since they do not agree with the measurements of the 2^{nd} volume. The choice of discarding this one and not the other is not well-founded. The measurements of the 2^{nd} volume agree with the pipette measured beforehand and there is no known reason in the operation of the detector, which could explain the increase between these two pipettes. A hypothesis is that the 3^{rd} was leaky. But a complete confirmation cannot be given.
The December pipette (No.10) consisted of ultra-pure xenon and was drawn after the science runs and the additional distillation phase. Only an upper limit at 90%

confidence limit is given due to the varying results. Between the measurements of pipette No.8 and No.10 maintenance was performed to solve the problem of the aforementioned small leaks in the interconnecting volume of V_{cal} and the pipette port, where the sample is stored between measurements. It could be possible that still a tiny leak remains, which could explain the increase in the tries of each volume. If this is the case and only two 1^{st} tries are used a krypton concentration of (0.054 ± 0.021) ppt results, as given in Tab. 1 bottom. Either way, this is the lowest krypton in xenon concentration in a running detector ever measured.

5.4.3 Krypton Concentration Evolution

In Fig. 20 the krypton concentration evolution of the XENON1T detector is shown.

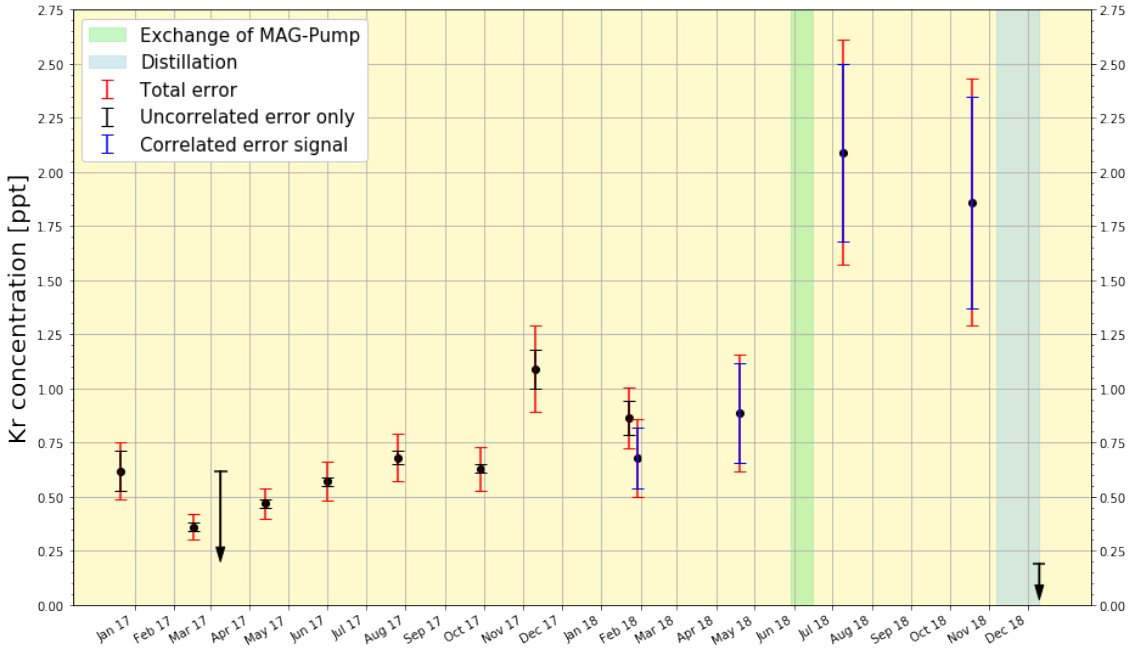

Figure 20: Krypton concentration evolution of the XENON1T detector. The data points with black error bars (statistical error) were evaluated with the standard procedure, the data points with blue error bars (systematic error on the signal) were evaluated with the procedure described in this thesis. Upper limits are shown with downward arrows, phases of operation are indicated by colored bands. Jumps in the krypton concentration can be explained by operations performed on the detector, indicated by colored bands.

Here also data points not evaluated in this thesis are shown. Until the measurement of the pipette taken in January 2018, the RGMS signal was understood and evaluated with the standard procedure described in Sec. 4.2.3 during the work of [60]. These points, therefore, have a statistical error (uncorrelated error) indicated by a black

error bar. The total error, including the systematic error (correlated error) due to the uncertainty of the krypton amount in the calibration gas, is shown by the red error bars. For the pipette measurements evaluated in this thesis (January 2018 onward) the statistical error was discarded and instead an additional systematic error due to the uncertainty of the true pedestal was introduced. In the plot, this error is indicated by the blue error bars. Similar to the other data points, the total error is marked by red error bars.
The pipette, taken in January 2018, was measured and evaluated twice at different times, therefore two data points in the plot. First, it was measured and evaluated with the standard procedure, while the chromatographic separation still worked. It was again measured after the problems mentioned before were resolved and the new signal evolution appeared. Consequently, the evaluation described in this thesis was applied. Even though the two values agree within their errors, the one evaluated within this thesis is substantially lower. Considering, that the front fit is always higher than the back fit, this might suggest that actually, the earlier data points and therefore the front fit are resulting in the true pedestal. Since this is the only pipette, which was measured with both signal evolutions, this can not be confirmed at the moment. Especially as it also might be possible that the 1^{st} volume (evaluated with the standard procedure) of the pipette had a tiny leak. This could then explain why the second measurement using the 3^{rd} volume (evaluated within this thesis) is lower. Further dedicated studies towards the signal evolution are necessary.
Measurements, where only an upper limit could be calculated, are reflected by a downwards arrow. Phases of relevant operations are indicated by colored bands. The exchange of a magnetic pump explains the increase after April 2018 to July 2018, since ambient air might have entered the system during the exchange. The possible introduction of a higher amount of krypton by filling additional new xenon was not the case as there is no increase between the July and October measurement apparent. After the science runs were finished, a distillation phase was started to clean the xenon before storing it for XENONnT. Afterward, the lowest krypton in xenon concentration ever measured in a running detector was achieved.

6 Adsorbent Characterization for Krypton-Xenon Separation

6.1 Motivation

As mentioned in Sec. 5.1, the RGMS had some problems in the chromatographic procedure, which resulted in a non-optimal separation of krypton from xenon and the analysis was not possible in a consistent way. Also, some of its properties make the currently used adsorbent (Chromosorb 102, see Sec. 4.2.2) not desirable to use in the future.
It is only heatable up to ∼170 °C, while higher temperatures lead to disintegration. Therefore, the bake-out after a measurement to remove all remaining krypton and xenon traces in the two columns T2 and T3 is limited. This can be troublesome for future measurements of samples, where the krypton impurity level is pushed down even further. This low temperature then either leads to longer bake-out times, which make a continuous operation more difficult or might even not be high enough to remove all krypton from T3.
Additionally, the separation power of Chromosorb is not ideal. As described in [59] for the standard procedure, krypton has left the separation column completely after ∼14 min, while xenon starts to leave the column after ∼50 min. Therefore, tailing of the krypton peak or fronting of the xenon peak can lead to an overlapping pass of krypton and xenon through the column, i.e. xenon starts to leave the column before krypton left it completely. This is called xenon breakthrough and ruins the separation and consequently the measurement. The xenon breakthrough is also triggered by a too large sample size, which can overload the adsorbent. As a result, the xenon is not retained as strong as before and reaches the end of the column earlier.
Last but not least, samples with a ppq (parts per quadrillion) krypton concentration require larger xenon sample sizes to comply with the sensitivity of the SEM. But this is in contradiction to the aforementioned separation power. Instead of a larger sample size also a bigger separation column could be used, but then the bake-out gets even more difficult.
For the above reasons, the purpose of this work is to find a better performing adsorbent to optimize the separation of krypton and xenon. Predicting selectivity characteristics of adsorbent columns is often a difficult task. It is known that krypton will have less retention than xenon, but how well adsorbent columns separate the two noble gases is often unclear. This is mainly due to the fact, that for the calculation of the Van-der-Waals forces, responsible for the adsorption, several approximations are necessary for the complex system of highly porous materials. The exact prediction of the adsorption equilibrium becomes consequently unfeasible. This can lead to significant deviations in realistic experimental conditions.
After an introduction to the basics of adsorption with focus on gas chromatography, a dedicated experimental setup to characterize and compare different adsorbent materials, based on their ability to separate krypton from xenon, is presented. Therefore several measurements of adsorption for different adsorbents have been carried out at different temperatures, carrier gas flow, and sample size.

6.2 Basics of Gas Chromatography

6.2.1 Overview on the Principles of Adsorption

The surface of a solid represents a discontinuity of its structure. The forces acting at the surface are unsaturated. Hence, when the solid is exposed to a gas (or liquid), the gas (or liquid) molecules will form bonds with it and become attached to the surface. The reverse process is called desorption. Some of the principal terms and properties associated with adsorption are defined in Fig. 21 and Tab. 2.
The solid itself is called adsorbent and has ideally a large specific surface area, i.e. adsorbents are highly porous materials. The total surface area is understood as the surface, including the pores, accessible for the gas or fluid from outside. The microporous structure can be characterized by standardized techniques. Depending on the internal width of the pores, they are subdivided by diameter d into macropores 500 Å$> d$, mesopores 20 Å$< d <$500 Å and micropores $d <$20 Å. The substance that is attached is called adsorbate when it is in the adsorbed state, but adsorptive as long as it is not bound on the adsorbent's surface. Moreover, for the adsorption onto surfaces, one distinguishes between chemisorption and physisorption. In the first case, adsorption results from chemical bonding between the adsorbate and the surface molecules of the adsorbent. This involves electron transfer, which is not the case for noble gases. Consequently, only physisorption plays a role in the following.

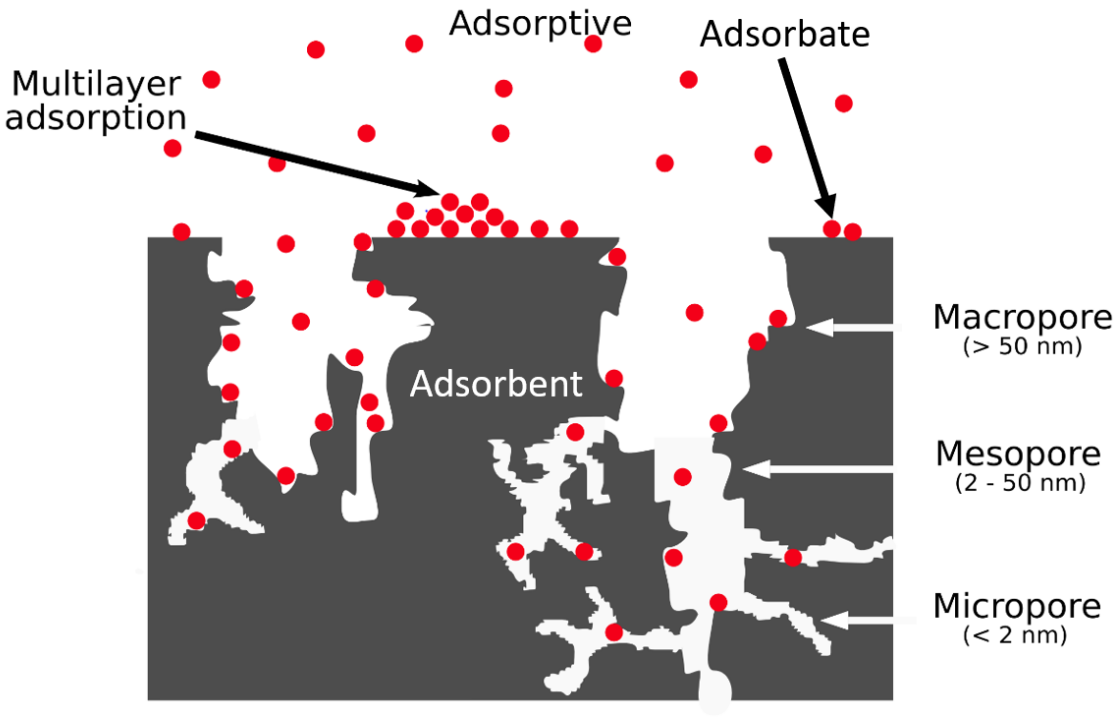

Figure 21: Terminology of adsorption on porous solids (adopted from [65]).

Term	Definition
Adsorption	accumulation of one or more components in an interfacial layer
Adsorbent	solid material on which adsorption occurs
Porous solid	solid with cavities/channels deeper than wide
Adsorbate	substance in the adsorbed state
Adsorptive	adsorbable substance in the fluid phase
Macropore	pore of internal width greater than 50 nm
Mesopore	pore of internal width between 2 and 50 nm
Micropore	pore of internal width less than 2 nm
Pore volume	volume of pores determined by stated method
Porosity	ratio of total pore volume to apparent volume of adsorbent
Surface area	extent of available surface as determined by a given method

Table 2: Terminology of adsorption used in literature (adopted from [65]).

In physisorption, the adsorbate is bound to the adsorbent only by weak intermolecular forces. These are van-der-Walls forces, induced instantaneously by dipole-dipole and higher multipolar interactions, and induction forces caused by a permanent electric field of the adsorbent material in case of a polar surface.
The most important relation in adsorption is the relationship between the partial pressure of the adsorptive and the amount of adsorbate. The relation at constant temperature between the amount of particles n adsorbed by the mass m of the solid and the partial pressure p of the adsorptive is known as the adsorption isotherm f_T, which depends on the composition of the gas (or liquid) solid *system*.

$$\frac{n}{m} = f_T(p, system) \tag{4}$$

The prediction of the isotherm is the task of the theoretical description of the adsorption. It is evident that assessment of the adsorption behavior is becoming complicated in the case of a multi-component system.
In this work an empirical study is carried out to find a better performing adsorbent for krypton xenon separation. Since the requirements solely focus on this special case and the predictive power of theoretical models is rather poor in this regard, the exact theoretical description of adsorption processes is of lesser importance. For this reason, a detailed description of theoretical models of adsorption is spared. For more information on the process of adsorption and also on various applications in industry and science one is referred to [66–68] or for a summary to [65, 69].

6.2.2 Overview of tested Adsorbents

In principle, all microporous materials can be used as adsorbents for gas purification and separation. However, the requirement for suitable adsorption capacity and separation power restricts the choice of adsorbents to those with well-controlled and high microporosity.
The most important characteristic of an adsorbent is its high porosity. Therefore, physical characteristics such as pore volume, pore size distribution, surface area, and density are generally of most practical importance. In Tab. 3 the used adsorbents in this work and their physical properties (as far as available) are presented.

Adsorber	max Temp. [°C]	particle size [µm]	surface area [m^2/g]	density [g/cm^3]
Chromosorb 102 [1]	170	149-177	300-400	0.29
Silica Gel [1]	1500	250-500	300	∼0.43
Molecular sieve 13X [1]	400	177-250	n/a	0.65
Molecular sieve 5A [1]	400	177-250	n/a	0.72
Charcoal 100085 [2]	450	∼ 450	159	0.43
Carbosieve SIII [1]	400	177-250	975	0.66
ShinCarbon [3]	300	149-177	1500	∼0.37
Adsorber	avg. pore size [Å]	pore volume[cm^3/g]	column height [cm]	column weight [g]
Chromosorb 102	85	n/a	6.2	0.66
Silica Gel	150	1.15	6.1	0.75
Molecular sieve 13X	10	n/a	6	0.98
Molecular sieve 5A	5	n/a	5.6	1.2
Charcoal 100085	∼ 22	1.17	6.1	0.84
Carbosieve SIII	4-11	0.35	6.1	1.25
ShinCarbon	n/a	n/a	6.2 / ∼24	0.65 / 2.55

Table 3: Overview of the tested adsorbents in this study. Their relevant physical properties as well as the the parameters of the column are given.
([1] Sigma Aldrich, [2] Blücher GmbH, [3] Shinwa Chemical Industries LTD)

The commonly used adsorbents can mostly be divided into five categories according to their chemical composition and will be presented in the following. Since adsorbents description, composition and synthetization is a topic on its own, more details on adsorbents, in general, can be found in [66–68, 70–72], here only the types of adsorbents are introduced.

Silica Gel
Silica gel is a synthetic amorphous and porous form of silicon dioxide. It is a rigid, continuous network of spherical particles of colloidal silica. Its surface is formed by Si-OH groups having a permanent polarization. As a result silica gel has a high capability to filter other polar molecules like water from mixtures. For this reason, Silica gel is most of the time used for drying. Several preparation methods exist, influencing the pore structure to have a characteristically strongly peaked pore distribution at a desired pore size.

Alumina
Alumina or activated alumina, a form of aluminum oxide, refers to (partially) dehydrated alumina hydrates in crystalline form with a high surface area. Similar to silica gel it is used for drying due to its hydrophilicity. It is commonly used in the drying of hydrocarbons.

Porous Polymers
Porous organic polymers are a large group of adsorbent materials with different surface areas and polarities owing to their different chemical composition. They are polyaromatic cross-linked materials with uniform rigid structures and synthesized by copolymerization of mono-functional monomers with difunctional monomers. Due to their low affinity to hydroxyl compounds, water elutes very quickly. A wide field of applications exists for this type of adsorbents, although not all factors contributing to the retention mechanism are fully understood. Various porous polymer beads are commercially available. *Chromosorb 102*, used in this study, belongs to this type of adsorbents.

Zeolites
Zeolites are crystalline aluminosilicates of alkali such as sodium, potassium and calcium. The crystal lattice has a uniform network of cavities and a high specific surface area. The pores are of molecular dimensions into which small enough molecules can enter and become adsorbed. This effectively sieves out molecules and hence they are often called *molecular sieves*. Since the micropore structure is determined by the crystal lattice it is precisely uniform with no distribution of pore size. This distinguishes zeolites from traditional microporous adsorbents. By varying the lattice structure, different types containing different sizes of pores can be prepared. Most commonly encountered are 4A, 5A, and 13X. Depending on the exact composition of the zeolites, the adsorption properties such as hydrophilicity can be influenced. Due to this flexibility, they can be designed for many applications in science and technology. The major application of molecular sieves is air separation for the production of nitrogen and oxygen, and hydrogen purification.

Activated Carbon
Activated carbons are characterized by a large surface area, which is among the largest of all absorbents. Activated carbon is normally made by thermal decom-

position of carbonaceous material (such as wood, peat, coals, bones, and coconut shell) followed by activation with steam at elevated temperature. The activation process involves essentially carbonization to eliminate the bulk of the volatile matter and then partial gasification to develop the porosity and surface area, thereby opening the pores. The conditions are carefully controlled to achieve the desired pore structure and mechanical strength. The structure of activated carbon consists of elementary microcrystallites of graphite. These are stacked together in random orientation and it is the spaces between the crystals which form the micropores. This system of partially split layers forms often slit-shaped pores. The pore structure may be pictured as having many small pores branching off from larger ones, which are open through the entire particle.
Activated carbon adsorbents generally show very little selectivity in the adsorption of molecules of different sizes. However, by special activation procedures, it is possible to prepare carbon adsorbents with a very narrow distribution of micropore size and which therefore behave as molecular sieves. Carbosieve SIII and ShinCarbon belong to this type.

6.2.3 Concepts of Gas Chromatography

Gas chromatography[1] is a method for separating components of mixtures to identify and determine the quantity of each component. The separation is achieved by one of these three mechanisms:

- Steric effects: The steric effect derives from the molecular sieving property. In this case, only small and properly shaped molecules can diffuse into the adsorbent, whereas other molecules are excluded.

- Kinematic effects: Kinematic separation is achieved by differences in diffusion rates of different molecules.

- Equilibrium effects: The different strength of the adsorption on surfaces by Van-der-Waals forces is used for the separation.

Due to the similar properties of krypton and xenon (e.g. the kinematic diameter Kr: 3.6 Å, Xe: 4.0 Å), steric and kinematic effects play a minor role. In the following the separation using different adsorption equilibria is explained first (based on the introductory chapters of [70–73]). Afterward, important measurement parameters within chromatography are discussed.

[1]Since this thesis is focused on the separation of krypton and xenon, details on liquid chromatography are not given. Even though, most of the relations presented in the following are valid also for liquid chromatography. Also, only gas-solid chromatography using an adsorbent packed column is introduced, since other variations and techniques are of less importance for the purpose of this thesis. For more information on the wide field of gas chromatography see [70–73].

Chromatographic Separation by Adsorption Equilibria

The central part is the chromatographic adsorption column, a long tube, packed with some adsorbent (in the following simply called column). The general concept of separation of gas components by gas chromatography is based on the transport of the sample through an adsorption column by using chemically inert carrier gases such as helium, hydrogen, nitrogen, or argon.

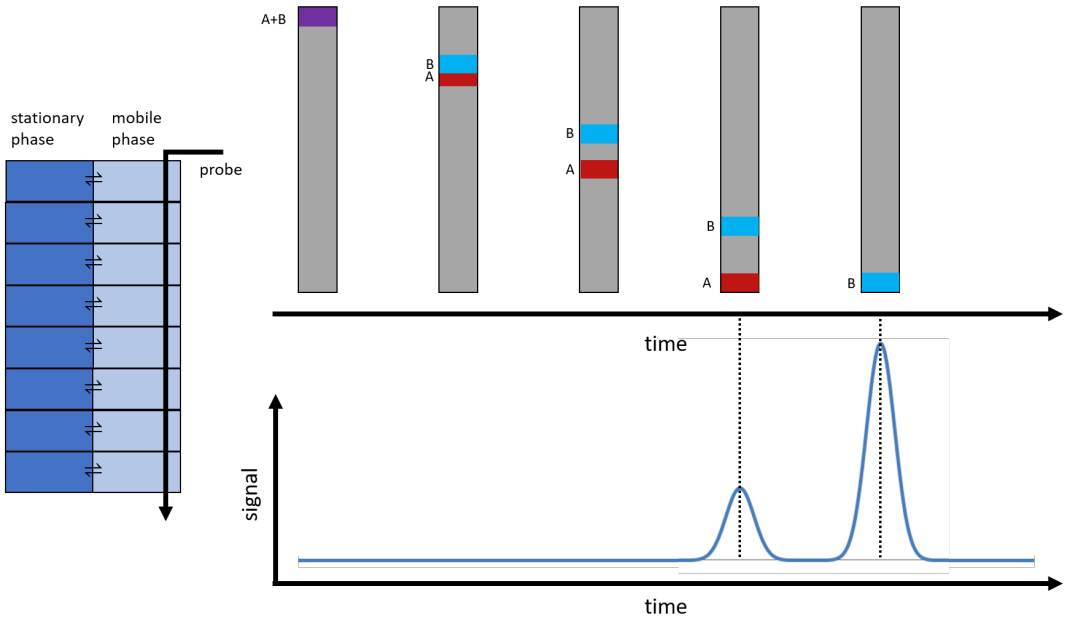

Figure 22: Illustration of the separation process - Left: the distribution into the stationary and mobile phase and the hypothetical sectioning of the column. In each stage, an equilibrium between the two phases is established, while the sample is pushed through the column. Top right: the separation of two components due to different velocities through the column is shown. The velocity depends on the adsorption properties of the component. Components adsorbed stronger exit the column at a later point of time. The signal over time, from a detector connected to the end of the column, results in the chromatogram illustrated at the bottom right.

The transport of a single component through the column is realized by distributing it between a mobile phase and a stationary phase. The adsorbent represents the stationary phase, whereas the mobile phase is the carrier gas, which passes continuously through the column at a constant velocity. The column can then be considered as a series of discrete sections, called theoretical plates. Each plate represents the theoretical distance required to establish an equilibrium between the stationary and the mobile phase. The distribution between the two phases is caused by adsorption processes, which are based on the van-der-Waals forces and the polarizability. The part of the analyte that remains in the equilibrated mobile phase is transported to the next plate by the carrier gas, i.e. adsorbed particles are transported in case of desorption before they are adsorbed again. Afterward, a new equilibrium is estab-

lished in both the first and second plate. The whole process is repeated with several theoretical plates until the end of the column.
The number of theoretical plates is one index used to determine the performance and effectiveness of columns. They are an indirect measure of peak width for a peak at a specific retention time and depend on the dynamic conditions in the column such as, for example, the flow rate or the diameter of the particles. The partition into these two phases and the series of discontinuous equilibrium plates are illustrated in Fig. 22 left. It is important to keep in mind that this model is an effective model of the chromatographic process. These plates do not exist and there are not actual distinct equilibria being achieved. More information on the theoretical description of the chromatographic process can be found in [70–73].
The chromatographic separation of a gas mixture of e.g. two components results due to different adsorption equilibria of the components. Depending on their adsorption properties, the gas components stay in the stationary phase for different times, which results in different migration rates of the analytes and consequently in analyte separation. The separation of two components is illustrated in the top right part of Fig. 22. First, the two analytes are not separated at all. Since component B is adsorbed stronger than component A, it stays longer in the stationary phase - the adsorbed state. Because of that, a larger portion of component A is pushed further by the carrier gas into the next plate, where a new equilibrium is established, while only a small portion of component B reaches the next plate. This is repeated in all plates resulting in an extension of the timely lead of component A in every plate. In other words, the components elute with different velocities through the column, depending on their respective adsorption properties. Consequently, the two components exit the column at different times.

Chromatogram and Measurement Parameters

The gas components are quantitatively measured by a detector connected to the column exit. The detector uses a physical or chemical property (e.g. electric conductivity or thermal conductivity) of the gas components by which they can be indicated. The detector current measured over time yields the chromatogram. In most analytical applications, all the required information can be obtained from the chromatogram. These are amongst others the purity of a sample, the identification of individual components of a mixture and a quantitative analysis of the mixture. An exemplary chromatogram is shown in Fig. 22 bottom right.
The x-axis represents the time and the y-axis the signal intensity. If only carrier gas reaches the detector a flat line is recorded, the so-called baseline. A gas component leaving the column is indicated by an increasing signal and results in a peak for each gas component eluted from the column. A peak is characterized by its position in the chromatogram and its height and width. Early peaks represent components that are only slightly retained in the stationary phase. The longer the components are retained in the stationary phase, the later they appear in the chromatogram. The time between the inlet of the sample and its maximum at the end of the column is

called retention time. The retention time of a component is itself a function of the many variables of the column operation. The peak positions within a chromatogram can be changed by altering the column temperature or the gas flow and the pressure of the carrier gas. Gas chromatography measurements are well reproducible because the peaks always occur at the same time with negligible variations. Further details about the gas chromatography technique can be found in [70–74].
The retention time refers to the maximum of a peak in the chromatogram. Other important parameters are peak width, peak asymmetry, and peak area as well as the resolution of two peaks for separation processes.
The shape of a peak is largely a function of the operation of the column. While it is being eluted from one end to the other, the sample gas band in the column broadens. This process is mainly attributed to the fact that the equilibrium of the gas between mobile and stationary phases does not take place instantaneously and diffusion of gas molecules occurs along the column axis. However, the position of the peak maximum is still related to the general equilibrium between the stationary and mobile phases. Other parameters which affect the peak shape and the peak broadening are finite mass transfer, and column geometry (e.g. the velocity of the carrier gas is uneven across the column cross-section, depending on the exact arrangement of the particles). There are several possibilities to define the peak width. In this work, the peak width at the half maximum (FWHM) is used. In theory, the result of the broadening in an ideal column is a Gaussian peak shape, but this is rarely observed in experimental data.
There can be many reasons for asymmetrical peaks. A common source for asymmetric peaks is the heterogeneity of the adsorbent surface. The binding energy of the available adsorption sites differs due to a broad pore size distribution (e.g activated carbon). The sites, which are energetically more favorable (higher binding energy), are occupied first. The following adsorbent particles can only occupy energetically less favorable places since the most favorable places have already been occupied. This means, however, that they are less firmly bound and desorbe more quickly, in contrast to the particles adsorbed at the more favorable sites with a relatively low desorption probability. Consequently, the strongly bound adsorbate particles remain behind the maximum of the peak when passing through the column and the peak gets a tail. This is called tailing. The opposite process, fronting, is also possible. In this case, the peak maximum is shifted relatively backwards. Peaks fronting occurs e.g. when the sample capacity of the column is exceeded. Another cause of peak fronting is channeling in a packed column. If narrow channels form in the stationary phase, some of the solute can get in front of the main part and can consequently elute slightly in front of the main peak, leading to peak fronting.
Usually, the concentration in the stationary phase and the mobile phase follows a linear distribution depending on the partial pressure of the adsorptive. However, if the sample quantity exceeds the maximum of the adsorber, called overloading, the linear regime is left, and the adsorption properties change. The peaks of an overloaded adsorbent column have a smaller retention time. Also, peak asymmetries may occur. Often large tailing is observed.

In general, the peak asymmetry is hard to predict due to different contributing effects such as temperature and geometry. Additional effects can lead to peak distortions, which result in tailing and/or fronting. Nevertheless, to characterize the asymmetry of the peaks in this work, two parameters are used (see Fig. 23). To evaluate the general asymmetry of the peak, an asymmetry factor A is calculated. Since predominantly tailing arises, additionally a tailing factor K is computed to compare different peaks in regard to their tailing:

$$A = \frac{b}{a} \quad , a(b)\text{: width from the front (back) @ 10\% to maximum} \tag{5}$$

$$A = 1 \text{ corresponds to perfect symmetry, while}$$
$$A > 1 \text{ indicates tailing and } A < 1 \text{ indicates fronting.}$$

$$K = \frac{b}{w} \quad , b(w)\text{: width from the back @ 10\% (half maximum to maximum)} \tag{6}$$

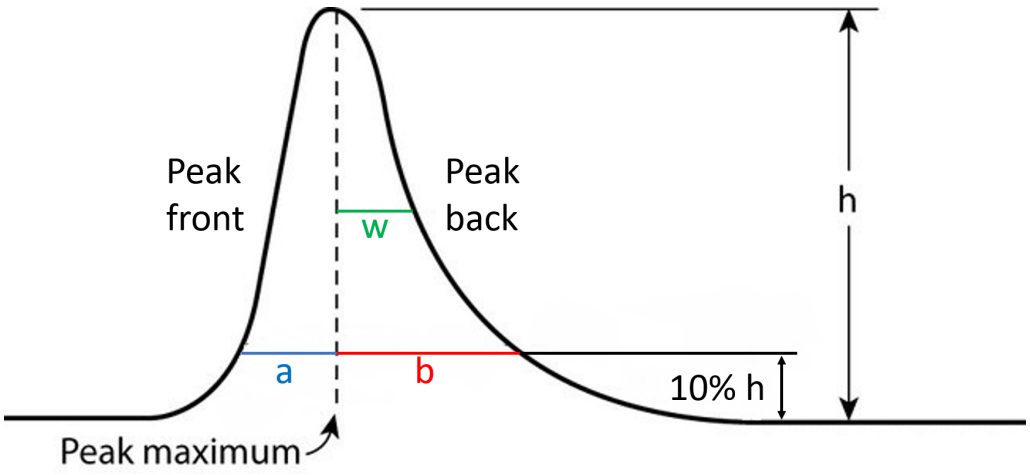

Figure 23: Illustration how the parameters are obtained, which are used to describe the asymmetry and the tailing of the peaks in this work.

Another important peak parameter is the peak area. The area of the peak in the chromatogram is a measure of the amount of gas and is important for quantitative gas chromatography. In this work, the chromatographic processes are only used for gas separation. The determination of the gas quantity is done in an independent second step and only used as a cross-check.
Up until now, only parameters were discussed to describe the peak of one analyte on its way through the column. However, chromatography is usually a tool to separate complex mixtures in order to identify the components of a sample. The degree of separation of an adjacent peak pair is described by the resolution R, defined as:

$$R = \frac{2(t_2 - t_1)}{1.7(w_{0.5,1} + w_{0.5,2})} \quad , \tag{7}$$

where t_x and $w_{0.5,x}$ are the retention times and the FWHM of peak x, respectively. $R = 1.5$ (6σ) indicates that the peak valley touches the baseline. The factor 1.7 arises due to using the FWHM.
Provided there is no instrumental deficiency, the separation of a given sample as it is recorded on the chromatogram is the basic measure of column efficiency. It is the result of the complex chromatographic process where stationary phase adsorbent interactions, column parameters, and conditions are interrelated. There exist several other parameters describing the column efficiency, peak shape, and retention times. In this thesis, one is mainly interested in the separation of krypton in xenon. In this respect, the discussion of column parameters increasing column efficiency is considered to be more important than the theoretical aspects.

6.3 Experimental Set-up and Measurement Procedure

A study to improve the stability of the RGMS was performed in [59]. There, the separation power of the Chromosorb column was investigated by connecting the output of the chromatographic system of the RGMS to a gas chromatograph. This is hardly feasible for the testing of different adsorption columns. The RGMS is an UHV-system, any contamination by opening the system should be avoided. Therefore, switching the columns regularly is not an option. Especially, since the RGMS should continue running and taking measurements. For this reason, a dedicated set-up was build, which can test adsorption columns independently, without interrupting the RGMS.

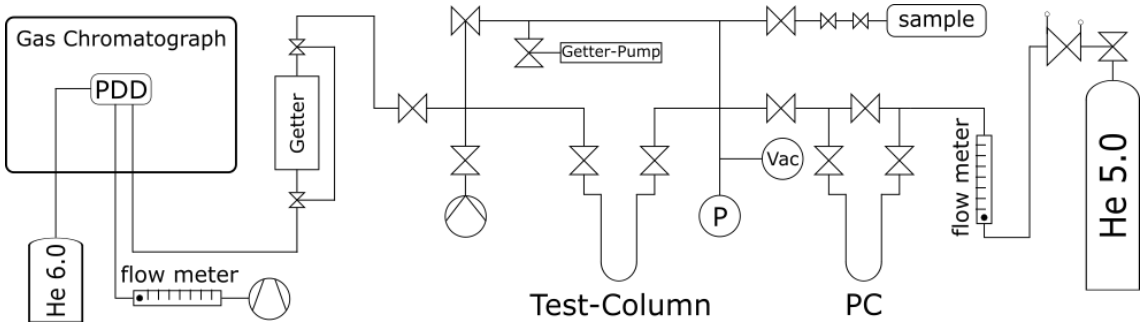

Figure 24: Schematic drawing of the experimental set-up. On the right-hand side the supply of the carrier gas including a charcoal column for purification (PC), in the middle the chromatographic system with the Test-Column and on the left the gas chromatograph for detection.

A drawing of the experimental set-up to characterize different adsorption columns is shown in Fig. 24. The basic elements are the supply of the carrier gas, the chromatographic system, as well as a gas chromatograph for detection. In Fig. 25 and Fig. 26 a picture of the set-up and a close view of the chromatographic system can be seen.

Figure 25: Picture of the experimental set-up. The gas-chromatograph on the left side, the getter and roughing pump on the bottom, below the chromatographic system. On the right hand side, the bottle supplying the helium is shown (credit: R. Lackner).

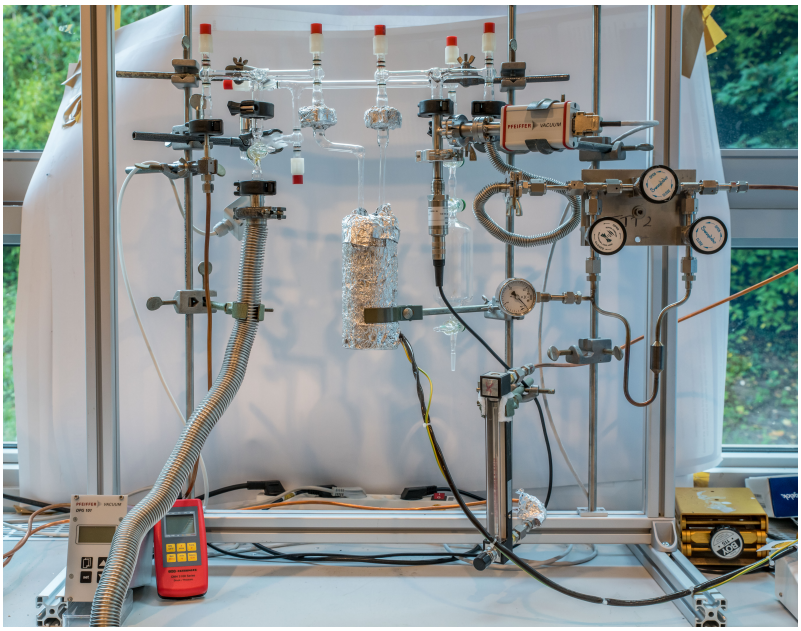

Figure 26: Picture of the chromatographic system. On the left are the connections to the getter and the pump. In the middle, the test column covered by a heating mantle is shown. On the right-hand side the column for purifying the helium flow, next to the pressure and vacuum gauges, as well as a flow meter can be seen. The getter pump is behind the pump connection and can not be seen in this picture (credit: R. Lackner).

Carrier Gas Supply

The used carrier gas is helium 5.0, which is provided by a bottle and regulated by a flow meter. It is further purified using an adsorbent filled packed column (Purification Column (PC), active charcoal) immersed in a liquid nitrogen bath.

Chromatographic System

The chromatographic system, made out of glass, consists of a second adsorbent filled packed column, called Test-Column (TC) with an inner diameter of 6 mm and a wall thickness of 1 mm, a volume to store the krypton in xenon sample, a roughing pump, a pressure and a vacuum gauge as well as a getter pump. The sample is separated from the rest by three valves containing small subvolumes, which are used to draw a certain amount of sample gas. The getter pump is necessary for the investigation of small sample sizes (10^{-3} regime). It is required to establish the vacuum down to 1×10^{-3} and maintain the vacuum during sample freezing (see measurement procedure). This avoids freezing of contamination onto the Test-Column. The Test-Column is connected by glass flanges and separated from the set-up by two valves. Therefore, it is easily exchangeable to test different adsorbents. Additionally, a valve is installed to bypass the Test-Column. An exemplary Test-Column is shown in Fig. 27. To hold the powdery adsorbent in the column, glass-wool on top and below the powder is fixed with punctures in the glass. During packing, the powder is pressed strongly together to avoid having voids between the adsorbent particles.

Figure 27: Picture of an exemplary column. Here filled with activated carbon. The adsorbent is fixed with glass-wool, so that the powder stays in place while carrier gas is flushed through the column.

Gas Chromatograph

A getter is used before the gas is transferred to the gas chromatograph. The getter is applied in addition to the getter pump to remove impurities from possible tiny air leaks during the chromatographic process, since the getter pump can not be operated at the applied pressure during the procedure and is thus closed off.
Afterward, the gas is analyzed by a gas chromatograph of type Trace GC Ultra from Thermo Fisher using a Pulsed Discharge Detector (PDD). It was customized and optimized for the measurement of impurities in xenon during two doctoral thesis [58, 75]. Even though it can be operated fully automatically using high-purity pneumatic 6-port diaphragm valves, as well as a so-called cryo-oven hosting a column, only its PDD is used in this set-up (for more details on the gas chromatograph see [75]).
To detect the elements at the outlet of the column, the gas is transferred to the PDD

[76, 77]. The gases are ionized by high energy photons [78]. A pulsed high voltage discharge is produced by two electrodes in a clean helium environment, flushed with a typical flux of ∼60 ml/min. In helium, the discharge triggers the forming of excited diatomic helium, which dissociates to the ground state of two single helium atoms by emitting high energy photons (13.5 eV to 17.5 eV). These photons are capable to ionize every compound/element except for helium and neon. After ionization of the analytes, the resulting electrons are focused toward the collector electrode, where the measured current constitutes the signal. This technique allows for the measurement of traces with concentrations at the ppb level [79]. The signal plotted over time then yields the chromatogram.

Measurement Procedure

To test different adsorbents for their separation of krypton from xenon, the set-up tries to imitate the chromatographic system of the RGMS. As a sample, a krypton-xenon mixture is used, which consists of 4.5% krypton 5.0 in xenon with a ppb level of impurities. The sample is frozen onto the test column and then a chromatographic procedure is performed (parameters depend on the tested adsorbent). The gas is constantly transferred to the PDD, which results in a temporal resolution of the gas components through the column, the chromatogram.
To make the different measurements consistent, the following general measurement procedure is applied:

- The PC is put in LN_2 and helium is flushed through the PC, TC-bypass, and getter-bypass. (∼20 min)
- Flushing is switched through the TC, which is still heated to make sure no contaminations are left in the column (∼20 min)
- The chromatographic set-up is pumped and the getter pump started (∼15 min)
- The TC is filled with over-pressure, closed, and then the TC is cooled to LN_2 temperature. The getter pump is set to the operating voltage to hold the vacuum in the set-up around the TC. This is done to avoid a contamination of the adsorbent from air leaks. (∼40 min)
- After the TC is pumped again, the sample is expanded into the volume between the TC and PC, where the pressure is measured. To get the desired sample size small sub-volumes are used.
- The sample is frozen on to the TC. (∼10-20 min)
- Flushing through the TC is started (getter pump closed and off). After the getter is on operating temperature, the desired flow adjusted and the baseline constant, the data acquisition is started.
- The baseline is recorded. (∼10 min)

- The LN_2 of the TC is changed to an ethanol-bath with a defined temperature. This equals $t = 0$ in the chromatogram.
- The measurement is stopped when the krypton and xenon peaks are recorded.

To prepare the set-up for the next measurement, the following preparations are done:

- The PC is heated first, while helium is flushed through TC- and getter-bypasses. (30 min)
- The heating is switched to the TC, flushing over PC- and getter-bypasses (20 min)
- Flushing of the TC is continued through the cold getter overnight.

Next, the general measurement is explained, before the analysis and results of the adsorbent investigation are presented.

6.4 Measurement

The selection of a proper adsorbent for a given separation is a complex problem. It involves finding the proper combination of the stationary phase and column construction for solving a particular separation problem. Most of the solids used as stationary phases have been developed for specific applications and it is not clear a priori whether an adsorbent is suitable for noble gas separation. Due to the similarities of the two noble gases, it is quite challenging to find a material that adsorbs xenon much more efficiently than krypton. The available information for krypton in xenon separation at the ppt level is scarce. Hence, it is essential to analyze and select the adsorbent very carefully to take advantage of differences in the adsorption properties. Since the behavior of an adsorbent is hard to predict, the general approach after installing a new column was the following:
The newly packed column is heated in a stream of carrier gas for at least 24 h to remove water, condensed from the atmosphere, and other volatile contaminants invariably contained in small quantities. After that, an initial test is performed with estimated operating conditions. If needed, several such survey runs are performed to have a clear separation of the krypton and xenon peak. Analytic methods for peak identification are not necessary, because the sample is quite pure, consisting only of xenon, krypton, and a minimal amount of argon. After the survey runs were successful, the operating conditions are adjusted to optimize resolution, retention time, and peak shape.
Besides the surface interactions of the adsorptive with the adsorption material, these are mainly influenced by:

- column length:
  The longer the column, the more theoretical stages are available. Consequently, the retention time is proportional to the column length. It should be

emphasized though that the resolution is proportional to the square root of the length. Also, peak broadening can be observed as well because of increased longitudinal diffusion inside the column.

- column diameter:
  Generally, the wider the diameter of the tube and the higher the amount of stationary phase per unit column length, the larger the maximum tolerable sample size. In principle, if a wide column is perfectly evenly packed, it would be equivalent to many narrow columns in parallel, and thus the efficiency of the column would be independent of the diameter. In practice, this is not the case and wide columns have a lower efficiency than narrow ones. E.g. flow-unevenness across a wide column occurs easily leading to a larger diffusion. Additionally, the temperature gradient increases for wider columns leading to different temperature zones within the column, which lowers the efficiency. The columns used in this work have an inner diameter of 6 mm.

- temperature:
  The temperature has two effects on the column efficiency. First, a higher temperature will lead to a higher gas velocity and consequently to an increased diffusion and ultimately to broader peaks. If one considers separation, the broadening of the peaks is most of the time outweighed by the change of the equilibrium conditions between the mobile and the stationary phases. As the temperature is reduced, the equilibrium is shifted towards the stationary phase, binding the adsorptive more easily. I.e. in equilibrium at a lower temperature, more gas atoms/molecules are adsorbed in the stationary phase. As a result, the retention times are increased. In simplified models, the retention values increase logarithmically with decreasing temperature.

- carrier gas velocity/flow/pressure:
  The velocity at which the analyzed gases are transported depends on the carrier gas flow. The faster the flow of carrier gas, the faster the gases move through the column. When two or more components are present in the sample, each usually behaves independently of the others, so that for a given carrier gas flow rate, the speed of each component will depend on the extent to which it is adsorbed. Since the column generally acts as a constant choke, a constant input flow will itself ensure a constant pressure on top of the column. To a first approximation, the retention time and the flow rate are inversely proportional as long as the pressure drop across the column is small.

- particle size and shape:
  Besides the pore structure of the adsorbent, also the size and the shape of the adsorbent particles influence the performance of a column by e.g. generating more flow resistance, presumably because smaller particles can fill the column with smaller voids. Overall, a smaller particle size yields better efficiency

and additionally less peak dispersion, since smaller particles lead to shorter diffusion path lengths.

- sample size:
  Generally, the sample capacity is proportional to the amount of stationary phase in the column. As mentioned before, overloading the column will result in poor performance, tailing, and a shift in retention times.

For a fixed column (diameter, length, adsorbent) the only parameters adjustable to influence the column efficiency are the temperature of the thermal bath and the flow of the carrier gas. The sample size is rather a parameter that one has to keep in mind to not overload the column.
For selecting operating conditions, it is generally desirable to maximize the resolution, subject to some restriction on the maximum acceptable measurement time. Details on the requirements, set in this work, are given in the analysis part in the next section.
But before getting to the analysis, some general remarks regarding the measurements are mentioned:
As one can see in Fig. 25, the tubing from the column to the PDD is rather long. Since this set-up is only used for testing and the final application for the column is the RGMS, where such tubing is not present (see Fig. 11), the flow time has to be considered. For this reason, a flow-time calibration was performed. The set-up (see Fig. 24) is altered momentarily by removing the pressure sensor and connecting the roughly pump at its port. At the previous pump port, which is right behind the Test-column, a septum is installed. After the desired flow is adjusted (measured at the output of the GC), a small amount of xenon is inserted with a syringe through the septum and the time after insertion until a signal at the PDD is apparent, is measured. This was repeated several times for two different flows F and the following flow-times were found:

- $(200 \pm 5)\,\mathrm{s}$ for $F = 40\,\mathrm{ml/min}$
- $(142 \pm 5)\,\mathrm{s}$ for $F = 70\,\mathrm{ml/min}$

Additionally, a blank test was performed. The change of the baseline is $\sim$1% and thus negligible.
To compare different sample sizes, a volume calibration is necessary to know the amount of sample frozen to the column. The calibration is performed by filling a small volume in front of the sample pipette (see Fig. 24), which has a known volume of 2 ml, with helium at pressure p. Then the set-up, except that volume, is pumped. By opening the small volume and releasing the gas into the volume V, where the sample gas is frozen to the column during the measurement procedure, a pressure drop is recorded. Using the ideal gas law, the volume V is estimated. This is repeated several times and the average is taken, resulting in $V = (0.107 \pm 0.003)$ ccmSTP with $p = 1\,\mathrm{mbar}$ sample.

6.5 Analysis

As mentioned in Sec. 6.2.3 the chromatogram is the result of the complex chromatographic process. The shape of chromatographic peaks depends on many experimental variables. As a consequence, the shapes of real chromatographic peaks can change considerably. The prediction of the peak shape is quite complicated since many of the parameters are unknown and incorporated in the processes happening as the gas is traversing through the column.
Therefore, it is almost impossible to theoretically derive an universal model that can describe all real chromatographic peaks. Finding a suitable model is therefore still a challenge. During this work, several common fit function of chromatographic peaks (taken from [80]) are used and tested if they can describe the measured peaks. These included the empirically transformed gaussian [81], exponentially modified gaussian [82] and several variations [83, 84], bi-gaussian [85], and poly-gaussian [86]. These fitting functions usually have 3 to 5 parameters. Fitting functions with more parameters were not considered since these have the disadvantage that most of the fitting parameters do not have any physical meaning, making it hard to use them for comparison of various peaks.
None of the tested fitting functions could describe the peaks in a consistent way, representing the front as well as the tail of the peak. Depending on the used fitting range either the front or the tail of the peak could not be described properly. Another problem is that some functions could also not fit the peak top reasonably, and the peak is overshot by the fitting function most of the time.
Since a usable fitting function to describe the measured peak forms in a consistent way could not be found, one has to rely on the raw data for the following analysis. To characterize the chromatographic peaks, the baseline is subtracted first. From the net signal, the peak parameters introduced in Sec. 6.2.3 are calculated. In comparing different adsorbent columns with respect to the goal of separating krypton from xenon, a column with optimal performance should have:

- maximal xenon retention
- reasonable krypton retention to avoid prolonging measurement time
- minimal krypton tailing and minimal xenon fronting to avoid possible overlapping of the peaks
- small krypton width which enhances separation
- resolution maximal
- baking of the column must remove all introduced xenon

In the next section, the results of measurements with different adsorbents are compared with regard to these requirements.

6.6 Results

In this section, the results of the aforementioned measurements are presented. First, the results of the initial version of the set-up are briefly mentioned and the reasons for updating the set-up are explained. Afterward, the results of the improved set-up are discussed.

6.6.1 Results of Initial Set-up

In the first version of the set-up, a different getter was used which only allowed small flows (F <14 ml/min). More precisely, the tubing of this getter has a tiny diameter, which requires a high input pressure to obtain the desired flow rate range. This is in contradiction to the limited pressure of such a glass set-up (∼1300 mbar).
At first, Chromosorb, which is already in use at the RGMS, is tested to confirm the measured parameters in [59]. However, the comparison with [59] is only possible to a limited extent due to the restricted flow rate of the set-up.
Basic gas chromatographic properties such as the increase of the retention times with lower temperature or lower flow rate are confirmed. Furthermore, a change of retention time with sample size is apparent, indicating that the column might be overloaded.
As a second adsorbent Silica gel (Sec. 6.2.2) is tested. Here the measurements show insufficient separation power within the adjustable parameters. For this reason, Silica gel is already ruled out for further investigations. The reason why Silica gel is worse in contrast to its given parameters (Tab. 3) could be the orientation of the molecule on the surface. The oxygen atoms surrounding the silicon as a tetrahedron could reduce the Van-der-Waals force.
Due to its limited flow-rate, which is too low in comparison to the flow used in the RGMS (∼40 ml/min), the getter was exchanged to the one shown in Fig. 25, allowing for flow rate in the l/min regime.

6.6.2 Results of the Improved Set-up

An exemplary chromatogram measured with the improved set-up using Chromosorb is shown in Fig. 28. A clear separation of the krypton peak, leaving the column first, and the xenon peak is apparent. The time at $t = 0$ corresponds to the change of the LN_2 bath to the thermal bath. The baseline is fitted using the time frame before $t = 0$ and is shown by the dark blue line. The temperature of the ethanol bath is measured manually multiple times during the measurement, the interpolation of the temperature curve is drawn in light blue. The peaks arising in the xenon peak are probably due to the change of the LN_2 level in the PC. Even though this measurement used the same flow and temperature bath as in [59], but a larger sample size (0.39 ccmSTP in comparison to 0.048 ccmSTP), the measured retention times do not agree. This indicates once again, that the column might be overloaded.

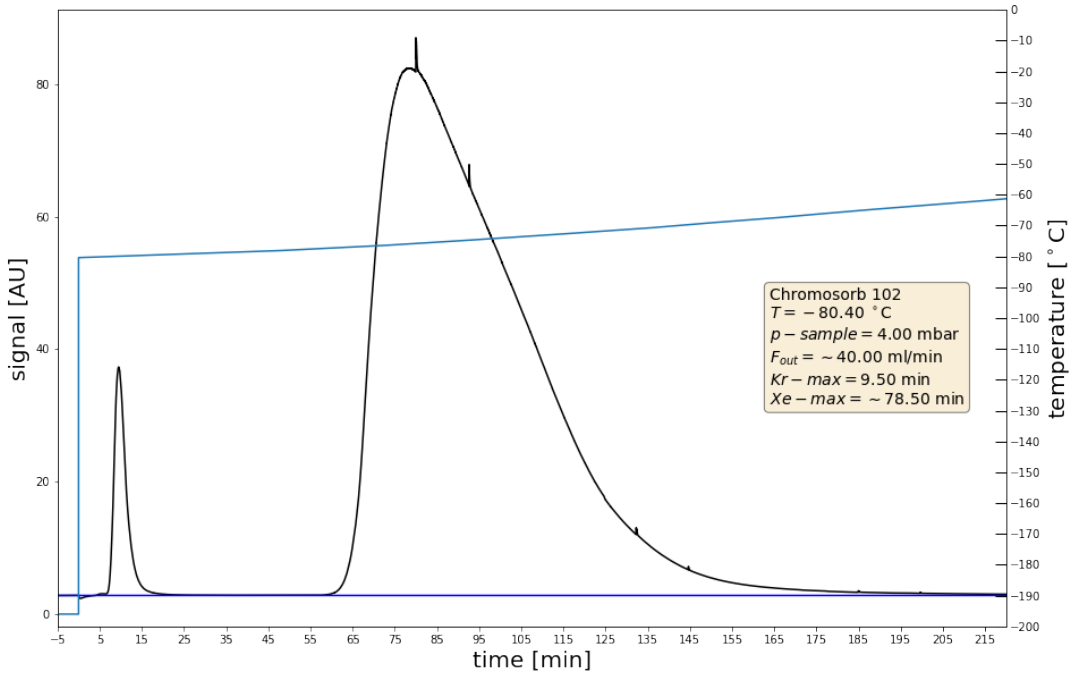

Figure 28: Exemplary chromatogram of Chromosorb. The time $t = 0$ corresponds to the change of the LN_2 bath to the temperature bath. The dark blue line indicates the fitted baseline. The light blue line shows the temperature curve of the test column i.e. the temperature of the thermal bath. The apparent peaks in the xenon peak are most likely due to the liquid level change of LN_2 at the helium column.

First, the results of the investigation of different adsorbents are presented. The results of the measurements with different adsorbents are shown in Tab. 4. All measurements were performed with the same sample size. Errors arise mainly due to the uncertainty of the flow rate as well as the temperature measurements.
In the first large column of the table, the measurement parameters are shown, in particular the used adsorbent, the adjusted flow of the carrier gas as well as the temperature of the thermal bath. In the next large column, the parameters discussed in Sec. 6.2.3 to analyze the krypton peak are presented. Next to the retention time, marked by "Max" in the table, these include the width corresponding to the FWHM, the asymmetry factor, which was defined as the width from the back at 10% to maximum divided by the width from the front at 10% to maximum. A value larger than 1 indicates tailing. Tailing refers to the asymmetry of a peak in chromatography in which the front part is steeper than the back part relative to the baseline. Since all measured peaks show tailing an additional parameter was introduced to investigate the fall off of the tail. This tailing parameter is defined as width from the back at 10% divided by the width from the half maximum to maximum (see Fig. 23). The larger this tail parameter, the larger the observed tailing of the peak. In the next large column, the results of the xenon peak analysis are shown. Xenon retention times above at least ∼3 h are indicated by an infinity symbol. In most cases, only

Parameter			Krypton				Xenon			
Adsorber	flow [ml/min]	Temp. [°C]	Max [min]	Width [min]	Asym	Tail	Max [min]	Width [min]	Asym	Resolution
Chromosorb	40±1	-80.4±0.3	9.5±0.1	2.9±0.1	2.0±0.1	2.4±0.1	78.5±0.1	38.1±0.1	4.2±0.2	3.7±0.2
Molecular sieve 13X	70±1	-80.0±0.3	7.6±0.1	1.8±0.1	1.8±0.1	2.3±0.1	83.3±0.1	26.8±0.1	1.4±0.1	3.5±0.2
	70±1	-60.0±0.3	4.9±0.1	1.5±0.1	2.4±0.1	2.4±0.1	∼18±2	-	-	-
	40±1	-59.7±0.3	8.3±0.1	2.8±0.1	2.0±0.2	2.4±0.1	46.7.0±0.1	18.4±0.1	1.5±0.1	2.4±0.2
Molecular sieve 5A	70±1	-80.4±0.3	11.1±0.1	3.0±0.1	1.5±0.1	2.2±0.1	132.5±0.2	39.5±0.1	1.2±0.1	3.5±0.1
	40±1	-80.5±0.3	19.5±0.1	6.6±0.3	1.5±0.3	2.1±0.1	189.0±0.1	48.9±0.2	1.3±0.1	3.6±0.1
Charcoal 100085	70±1	-80.4±0.3	61.1±0.1	17.6±0.4	1.4±0.2	1.9±0.1	"∞"	-	-	"∞"
	70±1	-60.6±0.3	18.9±0.1	6.0±0.2	1.5±0.2	2.0±0.1	"∞"	-	-	"∞"
	70±1	-31.3±0.3	6.6±0.1	1.9±0.1	1.7±0.2	2.3±0.1	-	-	-	-
	70±1	-18.8±0.3	6.2±0.1	1.7±0.1	2.0±0.2	2.3±0.1	46.0±0.1	21.3±0.2	4.1±0.1	3.6±0.2
Carbosieve SIII	70±1	-60.3±0.3	104.1±0.1	45.5±0.1	1.6±0.2	2.1±0.1	"∞"	-	-	"∞"
	70±1	-34.9±0.3	25.7±0.1	13.4±0.1	1.8±0.2	2.2±0.1	174±0.3	32.5±0.2	2.5±0.1	6.6±1.5
	70±1	-21.2±0.3	2.3±0.2	2.3±0.8	n/a	n/a	140.6±0.1	31.3±0.1	2.6±0.1	4.7±0.2
ShinCarbon	70±1	-60.7±0.3	25.8±0.1	7.9±0.1	1.4±0.1	2.0±0.1	"∞"	-	-	"∞"
	70±1	-40.5±0.3	10.5±0.1	2.8±0.1	1.6±0.1	2.1±0.1	194.4±0.1	53.2±0.1	-	5.7±0.1
	40±1	-40.3±0.3	16.8±0.1	5.6±0.1	1.5±0.1	1.9±0.1	277.0±0.3	76.9±0.2	-	14.4±0.3
	40±1	-25.4±0.3	11.6±0.1	3.7±0.1	1.7±0.1	2.2±0.1	155.2±0.1	58.4±0.2	-	3.6±0.1

Table 4: Evaluation of the tested adsorbents for krypton in xenon assays. The measurement parameters as well as the parameters describing peak shape and resolution are shown.

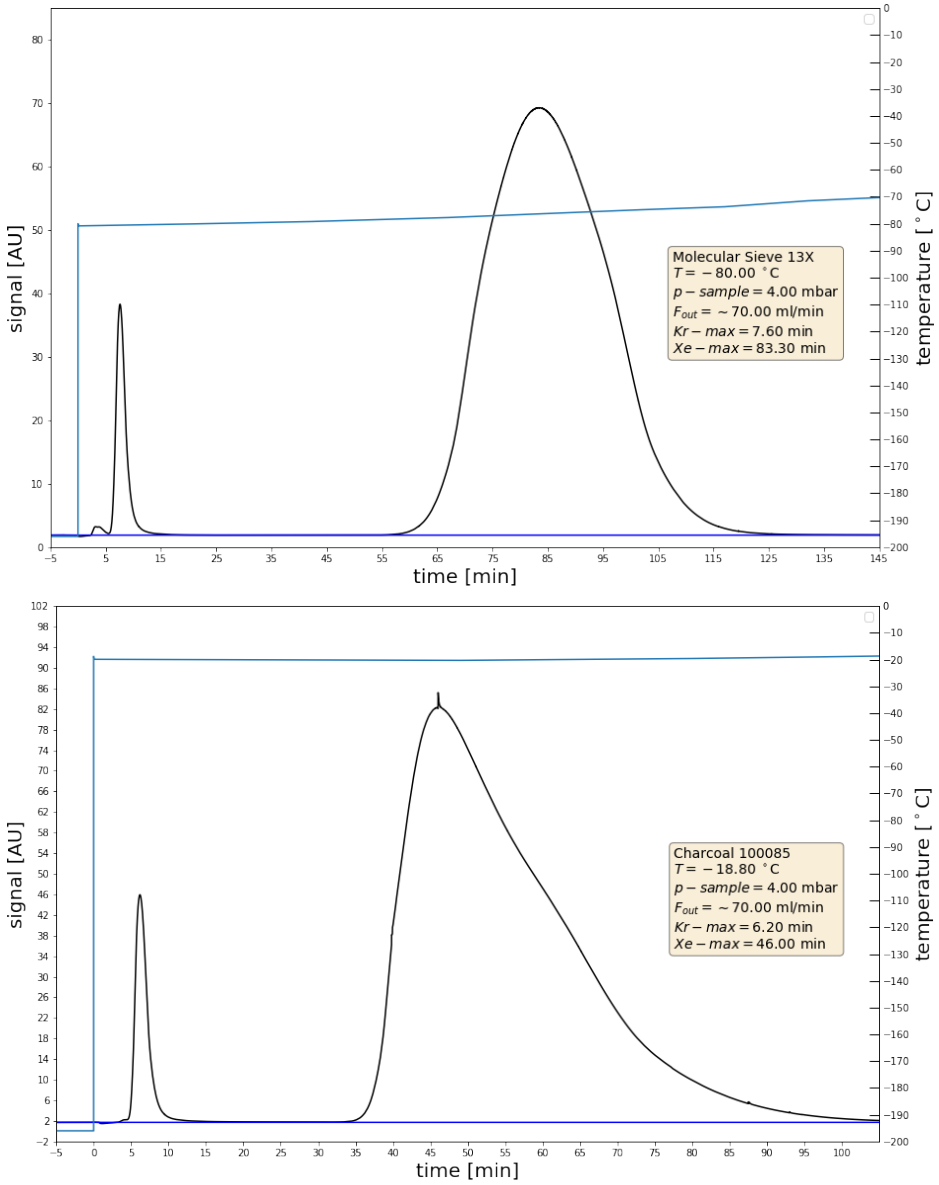

Figure 29: Exemplary chromatogram of molecular sieve 13x (top) and charcoal 100085 (bottom). Due to the homogeneous pore size of molecular sieves, the peaks are more symmetric, while active charcoals with a wide pore size distribution show tailing. The shown bumps in front of the krypton peaks are the remaining trace amount of argon in the sample. The dark blue line indicates the fitted baseline. The light blue line shows the temperature curve of the test column.

the rising edge of the xenon peak was recorded. Therefore, the asymmetry was not calculated, and the width was estimated by doubling the width of the front. In the last column, the resolution is presented. The resolution parameter describes the separation power of the complete chromatographic system relative to the particular components of the mixture. By convention, the resolution is expressed as the ratio of the distance between two peak maxima to the mean value of the peak width at the FWHM. The resolution is therefore one of the most important parameters for the analysis of krypton-xenon separation. Again, for xenon retention times above at least ∼3 h an "infinite" resolution is shown.
For all tested adsorbents, it seems that the lower the temperature of the thermal bath, the more symmetric are the krypton peaks. Due to the slower rise and a larger broadening, the peaks might get more symmetric. Simultaneously the tailing factor decreases. Because of the size of the error, a clear trend is not observable. Generally, the active charcoals have the highest retention times. One explanation is, that in the slit-shaped pores the intermolecular forces can act from two pore walls, binding the krypton and xenon atoms more strongly.
The xenon peaks for Chromosorb and the active charcoals exhibit a long tail with various bends. An exemplary chromatogram of a charcoal is shown in Fig. 29 (bottom). The tailing is not as strongly pronounced for the molecular sieves as one can already see by the asymmetry factor in Tab. 4 and by the plot in Fig. 29 (top). This is explained by the fact, that the molecular sieves have a homogeneous pore size, while active charcoals and other adsorbents have a wide pore size distribution.
Keeping in mind the requirements for a column with optimal performance, the active charcoals are favored over the molecular sieves due to their higher retention times and the better resolution. Even though charcoal 100085 shows good retention times and similar tailing and asymmetry in comparison to the other active charcoals, it is ruled out due to its coarse grain size (see Tab. 3). This precaution is taken, to avoid having problems due to voids between the particles in the column, which could differ significantly in another packed column.
This already leaves only two adsorbents in the closer selection: Carbosieve SIII and ShinCarbon. The Carbosieve adsorbent has a generally higher retention time, which is mainly due to its large density (see Tab. 3). This high retention time is actually counterproductive. The krypton retention time is in the range of 30 min to 100 min, depending on the temperature of the thermal bath. As this means, that the whole krypton peak takes at least about an hour to leave the column, this is not desirable in terms of measurement duration, krypton width, and energy consumption. To lower the retention time, either a higher flow or a higher temperature has to be used. For the aforementioned reason of pressure limitations in the set-up, a higher flow is not feasible. On the other hand, a higher temperature increases the asymmetry as well as the tailing as one can see in Tab. 3 for the three measurements of Carbosieve SIII. Even though the resolution gets worse for higher temperatures, it is still higher in comparison to Chromosorb or the molecular sieves. Nevertheless, the change of retention time of krypton is quite significant with moderate temperature change. This poses also the risk that variations of the temperature bath between

different measurements, intervenes with a controlled time frame of closing the column T2 in the RGMS measurement procedure (see Sec. 4.2.2). This makes the use of Carbosieve SIII overall not desirable.
In comparison to Carbosieve SIII, ShinCarbon has also large retention times, but for the krypton peak in a way more desirable range (10 min to 30 min). Also, the krypton peak has a small width, which enhances the separation. Additionally, the asymmetry and tailing parameters are among the lowest of all measurements. The xenon retention time is, even though generally smaller than Carbosieve SIII, still sufficiently large (in the range of 3 h). The resolution is in the same range as for Carbosieve SIII. Moreover, ShinCarbon is the first adsorbent to completely separate argon and krypton as shown in Fig. 30. Usually argon is apparent as a bump in front of or even completely incorporated in the krypton peak. This outstanding separation is most likely also working for krypton and xenon.

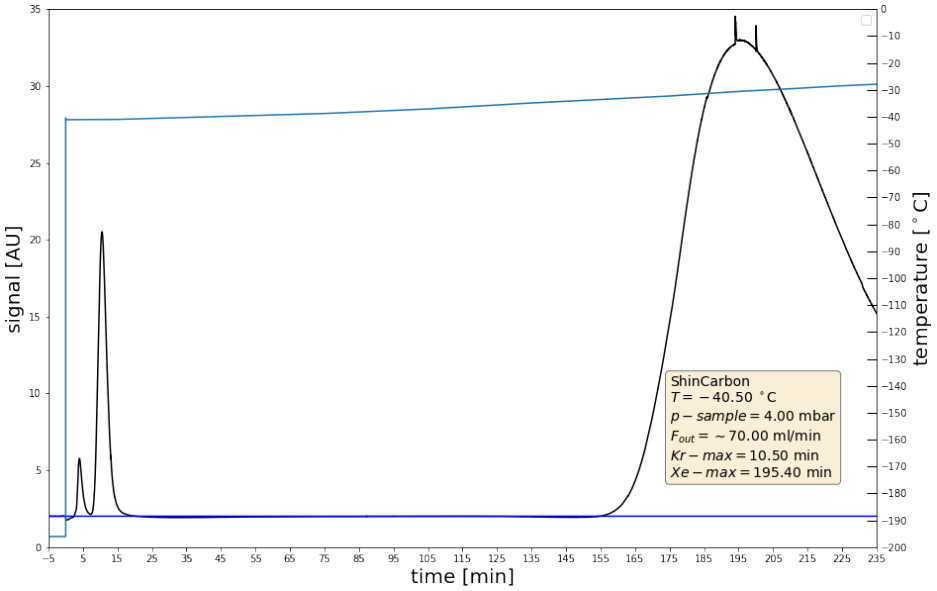

Figure 30: Exemplary chromatogram of ShinCarbon. The dark blue line indicates the fitted baseline. The light blue line shows the temperature curve of the test column. ShinCarbon is the only adsorbent, which could resolve the argon and krypton peak completely, showing its good separation power.

With all that said, ShinCarbon fulfills all tested requirements posed in Sec. 6.5. The point of removing all possible leftovers of xenon from a previous measurement by heating the column cannot be tested with the used set-up since the GC is not sensitive enough. Ultimately, this needs to be done by connecting the column to the RGMS. During the work of this thesis, this was not possible since the RGMS needed to continue performing measurements for XENON1T and XENONnT. A new updated system for the RGMS, called Auto-RGMS is currently in planning (see Sec. 7 for an outlook). The baking test will then be part of several performance tests of the new system at a certain stage of the project. Besides, one also has to

consider the following points. The ratio of the peak heights of the krypton and xenon peak are different by orders of magnitude for the RGMS samples (parts per trillion regime) and the sample used in this set-up (4.5% krypton in xenon). One has to make sure that this does not influence the performance of the column. Once again, this can only be tested by connecting the column to the RGMS.
Until now only a small sample size (∼factor 7 smaller than a typical RGMS sample) was used to avoid saturating the PDD. In the following the ShinCarbon adsorbent is investigated closer with regard to the sample size.

6.6.3 Closer Analysis of ShinCarbon

Since ShinCarbon has emerged as the best option, the next step is to test the performance using the same size of samples which is needed for the RGMS procedure. The performed measurements are shown in Fig. 31, where the chromatograms of the different sample sizes are overlaid. Due to the long measurement time (>5 h), the xenon maximum could not be recorded. Instead, the time of the xenon rise, defined as a signal 5% over the baseline, is used. The inset-plot shows the xenon rise time versus the sample size.
It is clear, that the expected independence of the retention time from the sample size is not the case. As one can see, the lower the sample size, the larger the xenon retention time. This could be problematic as the required sample size for the RGMS, displayed in the inset-plot by a grey line, lies in a non-constant region. In contrast to the xenon peak, the krypton maxima do not deviate from each other within their errors, which is illustrated by the blue line in the plot. The inset-plot in Fig. 31 implies that the region of constant retention time requires even smaller sample sizes.
In order to counteract this, a longer ShinCarbon column, with the parameters shown in Tab. 3, was produced. The column has about 3.9 times the mass and length. The results of the measurements performed with the longer column are shown in Fig. 32, where the chromatograms of measurements with different sample sizes are overlaid. The inset-plot shows the xenon rise time versus the sample size as above. The measured rise times are not quite consistent. The reason is that the definition of the rise as a signal 5% over the baseline gets inaccurate for such small sample sizes. The slowly rising peaks in combination with baseline noise complicate determining the exact rise time. This systematic error must be considered in interpreting the measured results. Moreover, small variations in the carrier gas flow, with regard to the long measurement time, could explain the discrepancy. Additionally, the temperature evolution of the thermal bath is displayed. The temperature curve is almost identical between the different measurements. As one can see in the plot, the krypton peak maintains to be unaffected by the sample size and the retention times agree within their errors. Considering the wide range of sample size used in the measurements and the mixture ratio of 4.5% krypton in xenon, a shift of the krypton peak should have been noticeable otherwise.

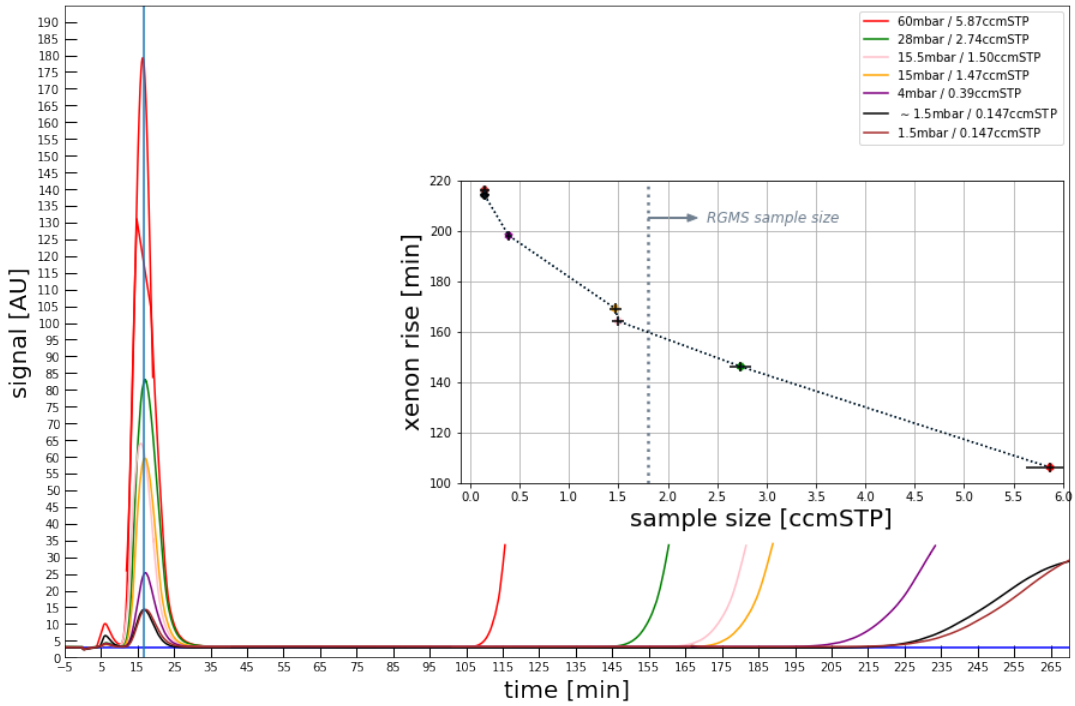

Figure 31: Overlaid chromatograms of measurements with different sample sizes using the ShinCarbon column. The inset-plot shows the xenon rise time versus the sample size. The required sample size for the RGMS is displayed by the grey line. It is clear, that the retention time of the xenon peak is not independent of the sample size, while the retention time of the krypton peak stays constant, illustrated by the blue line.

Since the smallest sample size in these measurements is already at the limit of the vacuum conditions of the set-up, a further reduction of the sample size is not possible and reaching a constant retention time region is not feasible. To exclude effects regarding influences between the gas components of the sample mixture, krypton and xenon must be tested separately. The measurement of the xenon only sample were done in this work and agree with the previous measurements. The test of a krypton only sample is still pending, but it is expected to not have an impact.
Furthermore, it was considered to test a column with a larger diameter. It is equally unlikely to expect that the issue is resolved with the available column dimensions and the used set-up. Also, other effects, such as the temperature gradient in the column, would make things even more complicated. Because of that, this idea is not pursued further.
The dependence of the xenon retention time to the sample size indicates that the column might be overloaded by the sample. An overloading effect by impurities and not the sample can be excluded due to the use of the getter pump. A possible overloading of the column does still not explain the constant retention time of the krypton peak, while the xenon peak is shifted with varying sample size. Considering

the wide range of sample size used in the measurements and the amount of krypton in the sample, a shift of the krypton peak should have been noticeable as well if overloading is the case. Instead, the krypton peak maintains to be unaffected by the sample size and the retention times agree within their errors. But the non-observed shift of the krypton peak could also be due to a not precise enough determination of the peak maximum. The timing of the change of the thermal bath is responsible for the uncertainty of t_0 and consequently for the position of the maximum. Effects regarding the influence of krypton to the xenon retention can be ruled out by xenon only measurements. Nevertheless, one can agree, that the constant retention time regime, independent of the sample size, is not reached. One possible explanation is overloading of the column, but this can not be confirmed with the measured data and other effects might also be possible.

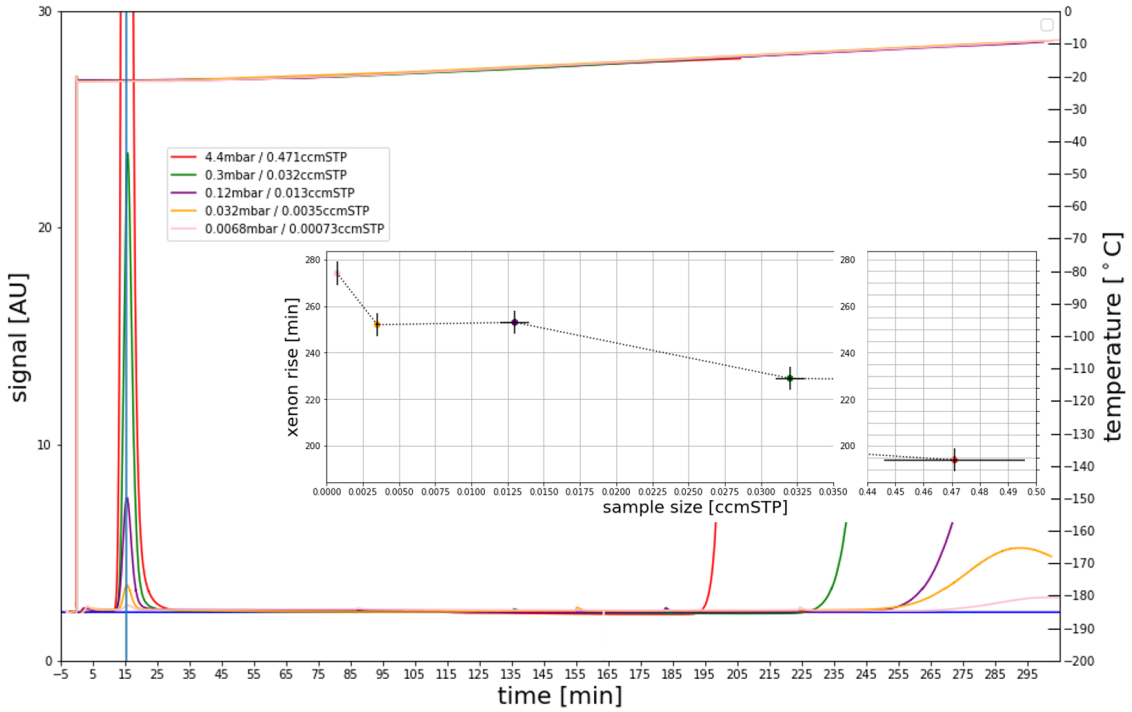

Figure 32: Overlaid chromatograms, including the temperature evolution of the thermal bath, of measurements with different sample sizes using the long ShinCarbon column. The inset-plot shows the xenon rise time versus the sample size. The retention time of the xenon peak is still not independent of the sample size, while the retention time of the krypton peak stays constant, illustrated by the blue line.

Cross-check of Chromosorb Column

Since one has found, that the ShinCarbon column is in a possible overloaded operation mode, this is also tested for the Chromosorb column as there were already some indications as mentioned in Sec. 6.6.1. The performed measurements are shown in

Fig. 33, where the chromatograms of the different sample sizes are overlaid. One can see that the shift of the xenon retention time is also the case here. This explains the xenon breakthroughs in past measurements, mentioned in Sec. 6.1. In these measurements, the sample size was above 2 ccmSTP. Comparing this with the measurement marked in yellow in Fig. 33, it is apparent that the peaks of krypton and xenon almost overlap at this sample size and a clear separation, as needed for the RGMS measurement, is not possible. This implies that the Chromosorb column is in a possible overloading operation mode as well. Avoiding the overloading of the column, while using a sample size necessary for the RGMS, is not feasible here as well.

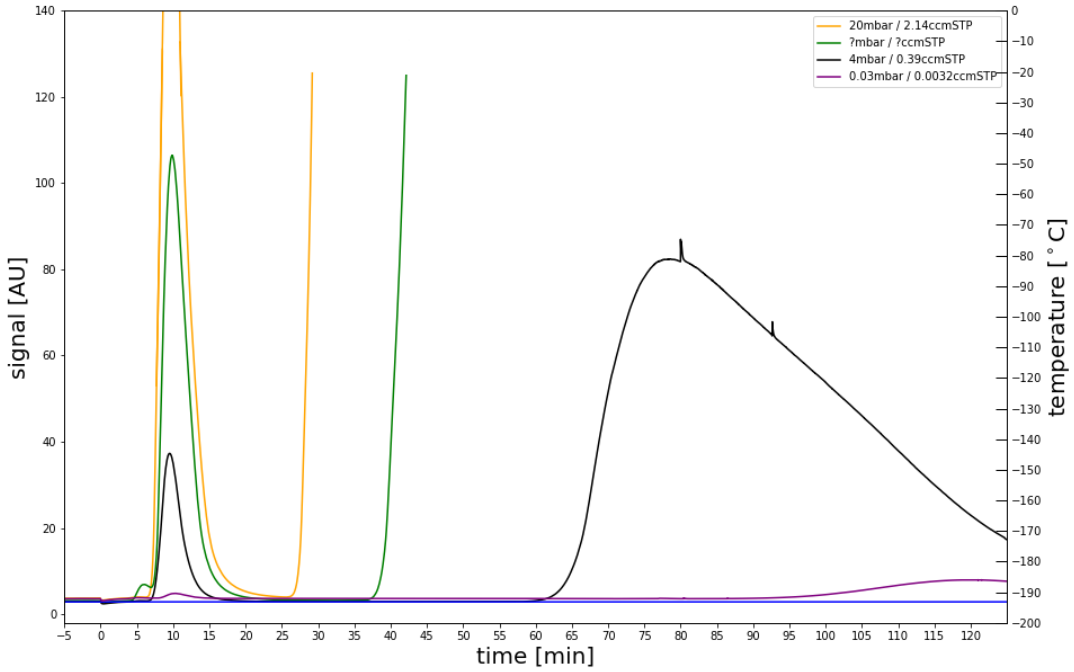

Figure 33: Overlaid chromatograms of measurements with different sample sizes using the Chromosorb column. The retention time of the xenon peak is not independent of the sample size, while the retention time of the krypton peak stays constant.

6.6.4 Column for the RGMS

The discussed results in this chapter show that the ShinCarbon adsorbent is ideal to be used in a column for the RGMS. It is heat-resistant up to 300 °C making bake-out more efficient as well as more secure in terms of overheating in comparison to Chromosorb. Moreover, the krypton retention time lays in a range, where the measurement time is not prolonged extensively. The krypton peak shows a small width and small tailing compared to other adsorbents, which, in addition to a large xenon retention, lead to the superior separation. Even though the column is in a

possible overloaded operation mode, the resolution is vast enough, that even large sample sizes do not interfere with the separation of krypton and xenon, and the danger of overlapping krypton and xenon peaks can be dismissed. Therefore, the ShinCarbon column can continue to be used, when krypton in xenon levels in the parts per quadrillion range, require large sample sizes to comply with the sensitivity of the RGMS. Last, the retention times are quite versatile and easily adjustable with the temperature of the thermal bath or the flow of the carrier gas, while keeping the aforementioned advantages. Thus, the ShinCarbon column can be adapted to the desired operating conditions of the new system, introduced in Sec. 7. The desorption efficiency of ShinCarbon, i.e. removing of all gas traces in the column by heating, remains to be tested with this new system.

7 Summary & Outlook

First, the krypton concentration in the XENON1T detector was investigated. The gas samples acquired in XENON1T from January 2018 onward and measured with the RGMS were re-analyzed. A change of the signal shape of the RGMS, whose origin is not fully understood, required a reconsidered analysis for these samples. For these measurements two regions in the signal appear, a grow-in/hill part at the beginning and a linear decreasing part at the end, which are not going smoothly into each other. Since it was not possible to determine, which data point region leads to the correct value for the introduced gas amount, a new analysis procedure was applied using two different fits, incorporating this not understood feature. A thorough and much improved error treatment was used to obtain the krypton concentration for different phases and operations of the XENON1T detector. Moreover, the krypton concentration evolution in the detector was determined, which included the lowest krypton in xenon concentration ever measured in a running detector. The obtained results are crucial input for the background model in the XENONnT experiment and will be used for future dark matter analyses.
In the second part of this thesis, a dedicated set-up was presented to test different adsorbents for their separation of krypton from xenon. The purpose was to find a better performing adsorbent to optimize the RGMS measurement procedure. Several adsorbents were examined and characterized for their usability in a gas chromatography column. Due to the posed requirements, such as optimal resolution, while having a reasonable krypton retention in terms of measurement time, the activated carbon ShinCarbon turned out to be the best candidate. The use of the ShinCarbon column will significantly improve the separation efficiency and the sensitivity of the measurement procedure.
The ShinCarbon column will be implemented in a upgrade of the RGMS to an automatized system, called AUTO-RGMS. Until now, a measurement takes roughly a day and has to be manually supervised and performed by an individual. For this reason, the RGMS is going to be completely remodeled. The AUTO-RGMS, will be equipped with computer-controlled pneumatic UHV-valves and other automated components, making the measurement procedure easier to handle and more consistent. With all planned updates, the AUTO-RGMS will able to measure an even lower concentration of krypton and is therefore ready for the future of direct dark matter detection using xenon.
While an increasing volume-to-surface ratio in larger xenon detectors causes a further reduction of the external background, the intrinsic background stays almost constant. Hence, it has the potential to be a crucial limiting factor on the experiments sensitivity. It will therefore still be necessary to monitor the krypton amount in the xenon target.
The obtained results for the AUTO-RGMS will be crucial to monitor the krypton background contribution of the ultimate liquid xenon dark matter experiment, called DARWIN. DARWIN will be using $\sim$50 t of xenon and is currently in its design phase [87].

References

[1] T. Marrodan-Undagoitia, L. Rauch, "Dark matter direct-detection experiments", *J. Phys. G43 (2016) no.1 013001* **2015**, DOI 10.1088/0954-3899/43/1/013001.

[2] J. Einasto, "Dark Matter", **2013**, DOI 10.1007/s13538-013-0147-9.

[3] G. D. Katherine Garret, "Dark Matter: A Primer", *Advanced Astronomy* **2011**.

[4] Particle Dark Matter, (Ed.: G. Bertone), Cambridge University Press, **2009**.

[5] F. Zwicky, "Republication of: The redshift of extragalactic nebulae", *General Relativity and Gravitation* **2008**, *41*, 207–224.

[6] V. C. Rubin, N. Thonnard, J. F. W. K., "Extended rotation curves of high-luminosity spiral galaxies", *The Astrophysical Journal* **1978**, *225*, L107.

[7] M. Bartelmann, P. Schneider, "Weak gravitational lensing", *Physics Reports* **2001**, *340*, 291–472.

[8] Y. Mellier, "Probing the Universe with Weak Lensing", *Annual Review of Astronomy and Astrophysics* **1999**, *37*, 127–189.

[9] D. Clowe et al., "A Direct Empirical Proof of the Existence of Dark Matter", *The Astrophysical Journal* **2006**, *648*, L109–L113.

[10] F. Kahlhoefer, K. Schmidt-Hoberg, M. T. Frandsen, S. Sarkar, "Colliding clusters and dark matter self-interactions", *Monthly Notices of the Royal Astronomical Society* **2013**, *437*, 2865–2881.

[11] D. J. Fixsen, "THE TEMPERATURE OF THE COSMIC MICROWAVE BACKGROUND", *The Astrophysical Journal* **2009**, *707*, 916–920.

[12] N. A. Bahcall, "The Cosmic Triangle: Revealing the State of the Universe", *Science* **1999**, *284*, 1481–1488.

[13] Planck Collaboration, "Planck 2015 results", *Astronomy & Astrophysics* **2016**, *594*, A13.

[14] W. et al, "Review of Particle Physics", *Journal of Physics G: Nuclear and Particle Physics* **2006**, *33*, 1–1232.

[15] V. Springel, C. S. Frenk, S. D. M. White, "The large-scale structure of the Universe", *Nature* **2006**, *440*, 1137–1144.

[16] V. Springel et al., "Simulations of the formation, evolution and clustering of galaxies and quasars", *Nature* **2005**, *435*, 629–636.

[17] J. W. Moffat, "Scalar–tensor–vector gravity theory", *Journal of Cosmology and Astroparticle Physics* **2006**, *2006*, 004–004.

[18] J. D. Bekenstein, "Relativistic gravitation theory for the MOND paradigm", *Phys.Rev.D70:0835092004; Erratum-ibid.D71:0699012005* **2004**, DOI 10.1103/PhysRevD.70.08350910.1103/PhysRevD.71.069901.

[19] A. M. Green, B. J. Kavanagh, "Primordial Black Holes as a dark matter candidate", **2020**.

[20] C. Alcock et al., "The MACHO Project: Microlensing Results from 5.7 Years of Large Magellanic Cloud Observations", *The Astrophysical Journal* **2000**, *542*, 281–307.

[21] M. Taoso, G. Bertone, A. Masiero, "Dark Matter Candidates: A Ten-Point Test", *JCAP 0803:0222008* **2007**, DOI 10.1088/1475-7516/2008/03/022.

[22] G. Jungman, M. Kamionkowski, K. Griest, "Supersymmetric Dark Matter", *Phys.Rept. 267 (1996) 195-373* **1995**, DOI 10.1016/0370-1573(95)00058-5.

[23] L. Visinelli, P. Gondolo, "Dark matter axions revisited", *Physical Review D* **2009**, *80*, DOI 10.1103/physrevd.80.035024.

[24] K. N. Abazajian et al., "Light Sterile Neutrinos: A White Paper", **2012**.

[25] O. Klein, "Quantentheorie und fünfdimensionale Relativitätstheorie", *Zeitschrift für Physik* **1926**, *37*, 895–906.

[26] G. Gelmini, P. Gondolo, "DM production mechanisms", *From 'Particle Dark Matter: Observations Models and Searches' edited by G. Bertone (Cambridge U. Press Cambridge 2010) Chap.7 p.121-141* **2010**.

[27] J. L. Feng, "Dark Matter Candidates from Particle Physics and Methods of Detection", **2010**, DOI 10.1146/annurev-astro-082708-101659.

[28] G. Bertone, "The moment of truth for WIMP dark matter", *Nature* **2010**, *468*, 389–393.

[29] V. A. Mitsou, "Overview of searches for dark matter at the LHC", *Journal of Physics: Conference Series* **2015**, *651*, 012023.

[30] V. Vitale, A. Morselli, "Indirect Search for Dark Matter from the center of the Milky Way with the Fermi-Large Area Telescope", **2009**.

[31] J. Lewin, P. Smith, "Review of mathematics, numerical factors, and corrections for dark matter experiments based on elastic nuclear recoil", *Astroparticle Physics* **1996**, *6*, 87–112.

[32] D. G. Cerdeno, A. M. Green, "Direct detection of WIMPs", *Chapter 17 of "Particle Dark Matter: Observations Models and Searches" ed. G. Bertone 2010 Cambridge University Press* **2010**, DOI 10.1016/j.nimb.2010.12.064.

[33] F. J. Kerr, D. Lynden-Bell, "Review of galactic constants", *Monthly Notices of the Royal Astronomical Society* **1986**, *221*, 1023–1038.

[34] T. Saab, "An Introduction to Dark Matter Direct Detection Searches and Techniques", **2012**, DOI 10.1142/9789814390163_0011.

[35] T. M. Giorgio Arcadi, "Lecture notes Dark Matter", **2019**.

[36] E. Aprile et al., "Dark Matter Search Results from a One Ton-Year Exposure of XENON1T", *Physical Review Letters* **2018**, *121*, DOI 10.1103/physrevlett.121.111302.

[37] J. Angle et al., "First Results from the XENON10 Dark Matter Experiment at the Gran Sasso National Laboratory", *Physical Review Letters* **2008**, *100*, DOI 10.1103/physrevlett.100.021303.

[38] E. Aprile et al., "The XENON100 dark matter experiment", *Astroparticle Physics* **2012**, *35*, 573–590.

[39] XENON Collaboration, "The XENON1T Dark Matter Experiment", **2017**, DOI 10.1140/epjc/s10052-017-5326-3.

[40] M. Ambrosio et al., "Vertical muon intensity measured with MACRO at the Gran Sasso laboratory", *Physical Review D* **1995**, *52*, 3793–3802.

[41] XENON collaboration, "Projected WIMP Sensitivity of the XENONnT Dark Matter Experiment", **2020**.

[42] E. Aprile, T. Doke, "Liquid xenon detectors for particle physics and astrophysics", *Reviews of Modern Physics* **2010**, *82*, 2053–2097.

[43] A. Lansiart, A. Seigneur, J.-L. Moretti, J.-P. Morucci, "Development research on a highly luminous condensed xenon scintillator", *Nuclear Instruments and Methods* **1976**, *135*, 47–52.

[44] LUXEvent, https://en.wikipedia.org/wiki/File:LUXEvent.pdf.

[45] L. S. Miller, S. Howe, W. E. Spear, "Charge Transport in Solid and Liquid Ar, Kr, and Xe", *Physical Review* **1968**, *166*, 871–878.

[46] XENON collaboration, "Conceptual design and simulation of a water Cherenkov muon veto for the XENON1T experiment", **2014**, DOI 10.1088/1748-0221/9/11/P11006.

[47] XENON collaboration, "Physics reach of the XENON1T dark matter experiment", **2015**, DOI 10.1088/1475-7516/2016/04/027.

[48] **2020**, home.cern/news/news/physics/xenon1t-reports-results-dark-matter-wimps-search.

[49] XENON Collaboration, "Removing krypton from xenon by cryogenic distillation to the ppq level", *Eur. Phys. J. C (2017) 77: 275* **2016**, DOI 10.1140/epjc/s10052-017-4757-1.

[50] E. Aprile et al., "^{222}Rn emanation measurements for the XENON1T experiment", **2020**.

[51] S. Lindemann, Master's thesis, University of Heidelberg, **2009**.

[52] J. Bieringer, C. Schlosser, H. Sartorius, S. Schmid, "Trace analysis of aerosol bound particulates and noble gases at the BfS in Germany", *Applied Radiation and Isotopes* **2009**, *67*, 672–677.

[53] S. Lindemann, PhD thesis, Max-Planck-Institut for Nuclear Physics Heidelberg, **2013**.

[54] E. Aprile et al., "Simultaneous Measurement of Ionization and Scintillation from Nuclear Recoils in Liquid Xenon for a Dark Matter Experiment", *Physical Review Letters* **2006**, *97*, DOI 10.1103/physrevlett.97.081302.

[55] XENON Collaboration, "Analysis of the XENON100 Dark Matter Search Data", *Astropart. Phys. 54* **2012**, DOI 10.1016/j.astropartphys.2013.10.002.

[56] S. Rosendahl, PhD thesis, Westfälische Wilhelms-Universität Münster, **2015**.

[57] M. Murra, PhD thesis, Westfälische Wilhelms-Universität Münster, **2018**.

[58] S. Lindemann, PhD thesis, University of Heidelberg, **2013**.

[59] D. Stolzenburg, Master Thesis, Max Planck Institut für Kernphysik Heidelberg, **2014**.

[60] L. Hoetzsch, Bachelor Thesis, Max Planck Institut für Kernphysik, **2016**.

[61] S. Lindemann, H. Simgen, "Krypton assay in xenon at the ppq level using a gas chromatographic system and mass spectrometer", *Eur. Phys. J. C (2014) 74:2746* **2013**, DOI 10.1140/epjc/s10052-014-2746-1.

[62] J. Hopp, M. Trieloff, R. Altherr, "Noble gas compositions of the lithospheric mantle below the Chyulu Hills volcanic field, Kenya", *Earth and Planetary Science Letters* **2007**, *261*, 635–648.

[63] E. de Hoffmann, V. Stroobant, Mass Spectrometry: Principles and Applications, **2007**.

[64] F. Froborg, A. R. Duffy, "Annual modulation in direct dark matter searches", *Journal of Physics G: Nuclear and Particle Physics* **2020**, *47*, 094002.

[65] S. Bruenner, Diploma Thesis, Max-Planck-Institut für Kernphysik Heidelberg, **2013**.

[66] Adsorption by Powders and Porous Solids, Elsevier, **1999**.

[67] R. T. Yang, GAS SEPARATION BY ADSORPTION PROCESSES, ICP, **1997**, 364 pp.

[68] D. M. Ruthven, Principles of Adsorption and Adsorption Processes, Wiley, **1984**, 460 pp.

[69] H. Simgen, PhD thesis, Universität Heidelberg, **2003**.

[70] A. B. Littlewood, Gas chromatography, eng, [by] A. B. Littlewood., Includes bibliographies., New York, **1970**.

[71] L. S. Ettre, A. Zlatkis, practice of gas chromatography, eng, edited by Leslie S. Ettre [and] Albert Zlatkis., Includes bibliographies., New York, **1967**.

[72] Practical Gas Chromatography, Springer-Verlag GmbH, **2014**.

[73] H. M. Mcnair, J. M. Miller, N. H. Snow, Basic Gas Chromatography, WILEY, **2019**, 288 pp.

[74] G. Guiochon, C. L. Guillemin, "Gas chromatography", *Review of Scientific Instruments* **1990**, *61*, 3317–3339.

[75] C. Hasterok, PhD thesis, University of Heidelberg, **2017**.

[76] W. E. Wentworth, S. V. Vasnin, S. D. Stearns, C. J. Meyer, "Pulsed discharge helium ionization detector", *Chromatographia* **1992**, *34*, 219–225.

[77] S. V. Vasnin, W. E. Wentworth, S. D. Stearns, C. J. Meyer, "Pulsed discharge emission detector — Application to analytical spectroscopy of permanent gases", *Chromatographia* **1992**, *34*, 226–234.

[78] H. Cai, W. E. Wentworth, S. D. Stearns, "Characterization of the Pulsed Discharge Electron Capture Detector", *Analytical Chemistry* **1996**, *68*, 1233–1244.

[79] W. Wentworth, H. Cai, S. Stearns, "Pulsed discharge helium ionization detector universal detector for inorganic and organic compounds at the low picogram level", *Journal of Chromatography A* **1994**, *688*, 135–152.

[80] V. B. D. Marco, G. Bombi, "Mathematical functions for the representation of chromatographic peaks", *Journal of Chromatography A* **2001**, *931*, 1–30.

[81] J. Li, "Comparison of the capability of peak functions in describing real chromatographic peaks", *Journal of Chromatography A* **2002**, *952*, 63–70.

[82] M. S. Jeansonne, J. P. Foley, "Review of the Exponentially Modified Gaussian (EMG) Function Since 1983", *Journal of Chromatographic Science* **1991**, *29*, 258–266.

[83] S. Purushothaman et al., "Hyper-EMG: A new probability distribution function composed of Exponentially Modified Gaussian distributions to analyze asymmetric peak shapes in high-resolution time-of-flight mass spectrometry", *International Journal of Mass Spectrometry* **2017**, *421*, 245–254.

[84] R. Delley, "Modifying the Gaussian peak shape with more than one time constant", *Analytical Chemistry* **1986**, *58*, 2344–2346.

[85] T. S. Buys, K. D. Clerk, "Bi-Gaussian fitting of skewed peaks", *Analytical Chemistry* **1972**, *44*, 1273–1275.

[86] J. R. Torres-Lapasio, J. J. Baeza-Baeza, M. C. Garcia-Alvarez-Coque, "A Model for the Description, Simulation, and Deconvolution of Skewed Chromatographic Peaks", *Analytical Chemistry* **1997**, *69*, 3822–3831.

[87] DARWIN Collaboration, "DARWIN: towards the ultimate dark matter detector", *JCAP 1611* **2016**, DOI 10.1088/1475-7516/2016/11/017.

Acknowledgments

Abschließend möchte ich mich bei allen bedanken, die diese Arbeit möglich gemacht haben. Für die Möglichkeit meine Masterarbeit am Max-Planck-Institut für Kernphysik schreiben zu können und Teil des XENON Experiments zu sein, möchte ich mich bei allen Beteiligten, insbesondere Herrn Professor Dr. Dr. Manfred Lindner, bedanken.
Zudem danke ich Frau Professor Dr. Stephanie Hansmann-Menzemer für ihre Bereitschaft, die Zweitkorrektur meiner Arbeit zu übernehmen.
Vielen Dank auch an alle meine Kollegen, die mir die tägliche Arbeit während meiner Zeit am MPIK sehr angenehm gemacht haben und für eine sehr entspannte und angenehme Arbeitsatmosphäre gesorgt haben.
Ein besonderes Anliegen ist es mir, mich bei meinem Betreuer Herrn Dr. Hardy Simgen zu bedanken. Während des letzten Jahres hat Dr. Hardy Simgen geduldig seine Erfahrungen mit mir geteilt, sowie mir hilfreiche Ratschläge in allen Belangen gegeben. Ich schulde ihm großen Dank für seine Unterstützung, die sich als wesentlich für die erfolgreiche Fertigstellung meiner Arbeit erwiesen hat.
Zu guter Letzt und am wichtigsten bin ich meinen Freunden und meiner Familie zutiefst dankbar. Ihre Unterstützung und Ratschläge spielten eine entscheidende Rolle für den erfolgreichen Abschluss meiner Arbeit.

Erklärung:

Ich versichere, dass ich diese Arbeit selbstständig verfasst habe und keine anderen als die angegebenen Quellen und Hilfsmittel benutzt habe.

Heidelberg, den 21.12.2020 .....